

11-2020

## Geomagnetic Aided Dead-Reckoning Navigation

Andrei Cuenca

Follow this and additional works at: <https://commons.erau.edu/edt>



Part of the [Aviation Commons](#), and the [Navigation, Guidance, Control and Dynamics Commons](#)

---

### Scholarly Commons Citation

Cuenca, Andrei, "Geomagnetic Aided Dead-Reckoning Navigation" (2020). *PhD Dissertations and Master's Theses*. 551.

<https://commons.erau.edu/edt/551>

This Thesis - Open Access is brought to you for free and open access by Scholarly Commons. It has been accepted for inclusion in PhD Dissertations and Master's Theses by an authorized administrator of Scholarly Commons. For more information, please contact [commons@erau.edu](mailto:commons@erau.edu).

# GEOMAGNETIC AIDED DEAD-RECKONING NAVIGATION

By

Andrei Cuenca

A Thesis Submitted to the Faculty of Embry-Riddle Aeronautical University  
In Partial Fulfillment of the Requirements for the Degree of  
Master of Science in Aerospace Engineering

November 2020

Embry-Riddle Aeronautical University

Daytona Beach, Florida

## GEOMAGNETIC AIDED DEAD-RECKONING NAVIGATION

By

Andrei Cuenca

This Thesis was prepared under the direction of the candidate's Thesis Committee Chair, Dr. Hever Moncayo, Department of Aerospace Engineering, and has been approved by the members of the Thesis Committee. It was submitted to the Office of the Senior Vice President for Academic Affairs and Provost, and was accepted in the partial fulfillment of the requirements for the Degree of Master of Science in Aerospace Engineering.

## THESIS COMMITTEE

---

Chairman, Dr. Hever Moncayo

---

Member, Dr. Richard Prazenica

---

Member, Dr. Eric Coyle

---

Graduate Program Coordinator,  
Dr. Marwan Al-Haik

---

Date

---

*Maj Dean Mirmirani*

---

Dean of the College of Engineering,  
Dr. Maj Mirmirani

---

Date

---

Associate Provost of Academic Support,  
Dr. Christopher Grant

---

Date

## ACKNOWLEDGEMENTS

This section is dedicated to all the great people I have met that help me throughout my professional and personal development to complete this important milestone in my life.

First, I dedicate this achievement to my father, mother, and sister, who encouraged me at the beginning of this path. I could not have begun this adventure without their love and support. You gave me more than I could even ask and guided me in the right direction.

My grandparents, who share their emotions with me on every step, even in the simplest ones, feel proud of what my sister and I are becoming. That fulfills me with great joy: their valuable wisdom and the unconditional love they share with us.

I want to thank my Advisor, Dr. Moncayo, for his valuable guidance and his invaluable assistance at every step during my Master's studies. His attention to my professional development and the projects I have been able to run under his direction. Without his trust and support, this accomplishment would not have been possible to complete.

My close friends, Carlos Zapata, who has been my pal, confidant, a partner in crime, emotional support, and, most especially, my best friend. Daniel Posada who gave me the motivation and valor to begin this adventure that represented a complete change in my life and how now I perceive the world. Giovanni Perez, who saw on me a potential I couldn't even understand at the moment, and advised me on important decisions in my life.

Eduardo Morillo helped me overcome many professional and personal obstacles that appeared along with this project development.

At last, thanks to all my friends and Coworkers at Embry-Riddle and The Advanced Dynamics and Control Lab for their quality time and immediate support.



## **ABSTRACT**

The dependence of modern navigation methods on global positioning systems has led to developing alternative algorithms for localization, capable of providing reliable and robust estimations. Global position system is commonly used in a vast majority of the world's devices, and it can supply real time position and velocity information. However, its accuracy can be compromised by external operational effects such as signal availability, cyber-attacks or weather conditions. This thesis investigates an alternative approach to enhance navigation in GPS-denied environments. Particularly, it develops an integrated navigation architecture based on geomagnetic referencing models capable of dead reckoning at GPS denied intervals. A geomagnetic matching algorithm combined with a nearest contour point of the magnetic surface is studied. Combined with an Extended Kalman filter as Inertial Navigation scheme, numerical simulations and experiments using on a quadrotor system are performed to assess the capabilities of the proposed approach at different navigation scenarios. A performance comparison between all the estimation methods is presented with the results section, and an overview of the influence of the vehicle in the measurements is presented along with the measurements gathered from experimental flights.

## TABLE OF CONTENTS

ACKNOWLEDEMENTS . . . . .	iii
ABSTRACT . . . . .	iv
LIST OF FIGURES . . . . .	vii
LIST OF TABLES . . . . .	x
ABBREVIATIONS . . . . .	xi
1. Introduction . . . . .	1
1.1. Thesis Objectives . . . . .	2
1.2. Thesis Outline . . . . .	3
2. Background . . . . .	5
2.1. Earth's Magnetic Field . . . . .	5
2.2. Coordinate Transformation . . . . .	7
2.3. Equations of Motion . . . . .	9
2.3.1. Vehicle's Dynamical Model . . . . .	10
2.4. Inertial Navigation System . . . . .	11
2.4.1. Bayesian Processing . . . . .	11
2.4.2. Kalman Filtering . . . . .	12
2.4.3. Extended Kalman Filtering . . . . .	14
2.5. Geomagnetic Aided Navigation . . . . .	15
2.5.1. High Altitude Navigation . . . . .	16
2.5.2. Low Altitude - High Range . . . . .	17
2.5.3. Low Altitude - Low Range . . . . .	18
3. Methodology . . . . .	20
3.1. Geomagnetic Map and Database Generation . . . . .	20
3.1.1. Uncertainty Area . . . . .	24
3.1.2. Correlation Analysis . . . . .	25
3.1.2.1. Minimum Difference . . . . .	25
3.1.2.2. Mean Absolute Deviation . . . . .	26
3.1.3. Geomagnetic Matching . . . . .	26
3.1.4. Nearest Euclidean Distance Point . . . . .	27
3.2. Inertial Navigation System . . . . .	28
3.2.1. Inertial Measurement Unit . . . . .	30
3.3. Extended Kalman Filter . . . . .	30
3.4. Simulation Environment . . . . .	31
3.4.1. Quadcopter Dynamical Model . . . . .	32
3.4.2. Quadcopter Control Model . . . . .	33
3.4.3. Trajectory Generation . . . . .	33
3.4.4. GAN Implementation . . . . .	34

3.4.4.1.	Sensor Models . . . . .	35
3.4.4.2.	INS - Extended Kalman Filter . . . . .	36
3.4.4.3.	Map Matching and Contour Approximation . . . . .	37
3.4.5.	Graphical Interface . . . . .	38
3.5.	Experimental Setup . . . . .	38
3.5.1.	Hardware . . . . .	39
3.5.2.	Software . . . . .	41
3.5.3.	Data Collection . . . . .	42
4.	Results and Analysis . . . . .	44
4.1.	Geomagnetic Fingerprint and Contour Lines . . . . .	44
4.2.	Trajectory Generation . . . . .	48
4.3.	Navigation Algorithms . . . . .	50
4.3.1.	Inertial Navigation System . . . . .	50
4.3.2.	Inertial Navigation System - EKF . . . . .	51
4.3.3.	GAN implementation . . . . .	53
4.3.3.1.	GMA with GPS . . . . .	54
4.3.3.2.	GAN with GPS . . . . .	55
4.3.3.3.	GAN with No GPS . . . . .	57
4.3.3.4.	Consideration of Failing conditions . . . . .	59
4.3.3.5.	GAN with Velocity measurement and No GPS . . . . .	61
4.4.	Experimental Data Observations . . . . .	63
5.	Conclusions and Future Work . . . . .	65
5.1.	Development of Geomagnetic Maps . . . . .	65
5.2.	Geomagnetic Aided Navigation . . . . .	65
5.3.	Experimental Implementation . . . . .	66
5.4.	Simulation Environment . . . . .	66
5.5.	Future Work . . . . .	67
	REFERENCES . . . . .	68

## LIST OF FIGURES

Figure	Page
1.1 MACE missile with ATRAN guidance (Mindling & Bolton, 2008). . . . .	2
1.2 Project Magnet RP-3D aircraft in 1994. . . . .	2
2.1 Dipole Representation of earth's Magnetic field with its magnetic and true North (Balay, 2018) . . . . .	5
2.2 Earth's core with its Magnetic flux lines (Lang, 2010). . . . .	5
2.3 Earth's Magnetic field vector Decomposition. . . . .	6
2.4 Inertial and body reference Frames . . . . .	7
2.5 Forces and moments acting in a quadrotor (Mian & Daobo, 2008) . . . . .	7
2.6 Gaussian Normal distribution and its probability regions (Galarnyk, 2019) .	13
2.7 Example of Geomagnetic Map and its corresponding contour lines . . . . .	15
2.8 Example of contour matching. Image extracted from (Duan et al., 2019) . .	16
2.9 Declination Map available at NOAA (Oceanic & Administration, n.d.). . . .	17
2.10 World Anomaly Magnetic Map (Oceanic & Administration, n.d.). . . . .	18
2.11 Fingerprints of the Magnetic components measures in (Storms, 2009) . . .	19
3.1 Geomagnetic Aided Navigation schematic proposed . . . . .	20
3.2 Testing Area at ERAU outdoor facility . . . . .	21
3.3 Microstrain 3DM-GX4-45 Sensor . . . . .	21
3.4 Sensor raw data and Calibrated Data . . . . .	22
3.5 Measured Magnetic Field's Magnitude map at Embry-Riddle Softball field .	23
3.6 Uncertainty Area boundaries . . . . .	24
3.7 MAD iteration 1 - Set up of each point . . . . .	27
3.8 MAD iteration 2 - First match. . . . .	27
3.9 MAD iteration 3 - Second match at same path. . . . .	27
3.10 MAD iteration 4 - Second match at different path. . . . .	27
3.11 Representation of the Nearest Distance point . . . . .	28
3.12 Strapdown Inertial Navigation System (Woodman, 2007). . . . .	28

Figure	Page
3.13 Simulation environment architecture . . . . .	31
3.14 3DR Quadcopter Available Selected for Testing . . . . .	32
3.15 3DR CAD model Representation built in Autodesk Inventor . . . . .	32
3.16 Simulink Blocks implemented for the Quadcopter dynamics . . . . .	32
3.17 NLDI Controller Architecture (Rivera, 2018) . . . . .	33
3.18 NLDI blocks implemented in the Simulation environment . . . . .	34
3.19 Control allocation block as interconnection block . . . . .	34
3.20 Decomposed Time-dependent Trajectory . . . . .	34
3.21 Magnetometer Sensor model . . . . .	35
3.22 GPS Sensor model . . . . .	35
3.23 Three-axis inertial measurement unit in Matlab's Navigation Toolbox . . . .	36
3.24 Extended Kalman filter block . . . . .	37
3.25 GAN Simulink blocks architecture . . . . .	37
3.26 Graphic interface Visualization . . . . .	38
3.27 PX4 V4 Autopilot. . . . .	39
3.28 PX4 Pixhack V5 Autopilot . . . . .	39
3.29 T-Motor MT 2216-9 1100kV . . . . .	39
3.30 T-Motor 10x3.3 Propellers . . . . .	39
3.31 3DR Quadcopter Setup . . . . .	40
3.32 Mission planner interface (Ardupilot, 2020) . . . . .	41
3.33 Simulink block for Microstrain data reading. ADCL Implementation . . . .	42
3.34 Collection data Flight performed at Embry-Riddle's Softball Field . . . . .	42
4.1 Indoor Facility - Magnetic field measurements. . . . .	44
4.2 Indoor Facility - Point locations experiment Results. . . . .	45
4.3 Probability density function observed from the Geomagnetic Map . . . . .	46
4.4 Interpolated Field's Magnitude map from data of Figure 3.5 . . . . .	47

Figure	Page
4.5	Approximated Field's Magnitude map from data of Figure 3.5 . . . . . 47
4.6	Measured and approximated contours . . . . . 48
4.7	Trajectories proposed as study cases. a) O pattern, b) S pattern . . . . . 49
4.8	Position References for trajectory O . . . . . 49
4.9	Position References for trajectory S . . . . . 49
4.10	INS results for positions and velocities with gyro and accelerometer data . . 50
4.11	Trajectory O - EKF Position Estimation . . . . . 51
4.12	Trajectory O - States estimated by the EKF . . . . . 52
4.13	Trajectory S - EKF Position Estimation with GPS measurements . . . . . 53
4.14	Trajectory S - States estimated by the EKF with GPS measurements . . . . 53
4.15	Trajectory S - Geomagnetic Matching Position estimation . . . . . 54
4.16	Trajectory O - Geomagnetic Matching Position estimation . . . . . 55
4.17	Closest Contour Point representation . . . . . 56
4.18	Trajectory O - 3D Visualization of GAN Path estimation . . . . . 56
4.19	Trajectory S - 3D Visualization of GAN Path estimation . . . . . 57
4.20	Trajectory S - Geomagnetic Aided Position Estimation . . . . . 57
4.21	Trajectory O - Geomagnetic Aided Position Estimation . . . . . 58
4.22	Trajectory O - GAN Position Estimation with no GPS at 11s-30s . . . . . 58
4.23	Trajectory S - GAN Position Estimation with no GPS at 11s-30s . . . . . 59
4.24	Trajectory S - INS and EKF estimation comparison . . . . . 60
4.25	Flat Magnetic Area detected by the uncertainty area . . . . . 61
4.26	Trajectory S - INS and EKF Est. comparison with velocity measurement . . 62
4.27	Trajectory S-GAN Est. with velocity measure/GPS drop at 12s-30s . . . . . 63
4.28	Trajectory O-GAN Est. with Velocity measure/GPS drop at 12s-30s . . . . 63
4.29	Flight test Magnetic Data . . . . . 64

## LIST OF TABLES

Table	Page
3.1 Microstrain Magnetometer Sensor specifications . . . . .	22
3.2 Microstrain Accelerometer/Gyroscope Specifications . . . . .	40
3.3 PX4 V4 Accelerometer/Gyroscope Specifications . . . . .	41
4.1 Reduced Chi-Squared Goodness-of-fit Metric . . . . .	46
4.2 Error Metric Table of Estimator's performance . . . . .	62

**ABBREVIATIONS**

ADCL	Advanced Dynamics and Control Laboratory
GNSS	Global Navigation Satellite System system
GPS	Global Positioning System
INS	Inertial Navigation System
GAN	Geomagnetic Aided Navigation
ICCP	Iterative Closest Contour Point
NED	North, East, Down
IMU	Inertial Measurement Unit
EKF	Extended Kalman Filter
UKF	Unscented Kalman Filter
PF	Particle Filter
PDF	Probability Density Function
PROD	Product Correlation Algorithm
NPROD	Normalized Product Correlation
MAD	Mean absolute deviation
MSD	Mean Variance Algorithm
NEDP	Nearest Euclidean Distance Point



## 1. Introduction

Increasing dependence on Global Navigation Satellite Systems (GNSS), along with its intrinsic reliability, has led society to look into developing new methods for navigation that can adapt to different conditions and environments where satellite positioning is not the best option. Nowadays, most navigation systems are built around the global positioning system (GPS) since it can return positions and velocities with high precision. Despite this, GPS based methodology is susceptible to errors due to external causes as jamming, occlusion, or lack of reachability.

Researchers have been working on alternatives to compensate for GPS navigation weaknesses, from inertial navigation to quantum clocks. One of those alternatives proposed before the GPS era is the terrain navigation technique based on contours. Back in 1940, Goodyear Aircraft corp. Started developing the Automatic Terrain Recognition and Navigation System (ATRAN), a radar-map matching system that was capable of correcting the flight path deviation by correlating measurements from a radar scanning antenna with a series of maps on board a missile. Later in 1958, this was successfully demonstrated at Holloman AFB (Goldenber, 2006) by using a three-axis precision magnetometer attached to plane and finding the best fit between the geomagnetic profile measured during the flight, and the corresponding profile in a stored map. With it, a foundation for modern geomagnetic navigation was established.

Once terrain information was proven to be highly reliable for navigation, terrain maps constructed years before were used for conceptual proofs and testings. The company E-systems pioneered terrain navigation implementations and developed a successful terrain contour matching system known as TERCOM in 1973. The company conducted experiments using maps made in 1895, which was sufficiently similar to the vertical profiles measured at the test to achieve a match (Goldenber, 2006). Around the same concept, E-systems developed an abnormal contour matching system based on geomagnetism, called MAGCOM, and the use of geomagnetic anomaly data was carried out as terrain map.

Due to the interest of military agencies in alternative navigation methods, the subsequent developments of geomagnetic contour matching systems were conducted by the US navy under the project MAGNET. The MAGCOM project faced mapping the areas of interest while the government had the required technology to provide maps of geomagnetic anomalies. The project MAGNET was a major geomagnetic survey effort from 1951 through 1994 led by the U.S. Navy Hydrographic Office using aircrafts as shown in Figure 1.2. The data collected was used to support the navigation of aircraft and ships while continuing scientific research (Chang, 2017).



*Figure 1.1* MACE missile with ATRAN guidance (Mindling & Bolton, 2008).



*Figure 1.2* Project Magnet RP-3D aircraft in 1994.

Although research around the use of the Earth geomagnetism as a navigation tool has continued over the years, its main attention was taken once GPS technology showed its tremendous achievements. GPS significantly marked an era in navigation accuracy and returned a strong foundation in mapping, and once its vulnerable characteristics were discovered, it forced the navigation entities to look back for alternative Navigation methods such as the geomagnetic contour matching.

### **1.1. Thesis Objectives**

The main purpose of this research is the development of a position estimator by integrating an Inertial Navigation System (INS) with a geomagnetic referencing model, capable of dead reckoning at GPS denied intervals, better known as Geomagnetic Aided

Navigation (GAN). This will form the bases to understand how geomagnetic data can be used to support localization methods, and will set conclusions over its efficiency and reliability under certain conditions. To achieve this goal, several elements have been identified and are summarized as follows:

- Database survey and adequacy of the geomagnetic map
- Geomagnetic matching algorithm definition
- Inertial Navigation System definition
- Geomagnetic Aided Navigation Algorithm definition
- Evaluation of concepts through actual implementations

This document will present a detailed explanation of each of these elements through each chapter's development and explain how they are connected and integrated in a geomagnetic aided navigation algorithm.

## **1.2. Thesis Outline**

The proposed research document opens with the Background in Chapter 2, where mathematical and theoretical concepts required to understand and design the algorithms are presented. This concepts includes the geomagnetic phenomena, vehicle dynamics and equations of motion, definition of Bayesian processing and its development into Kalman filtering, and the a definition of different scenarios were Geomagnetic Aided Navigation can be applied.

Chapter 3 covers the methodology based on the defined the specific objectives, starting with the geomagnetic map generation from survey data and intermediate processes as interpolations and polynomial approximations to adequacy of the data set. Once the map is generated, the geomagnetic matching algorithm is defined based on correlations rules and a position estimator based only on magnetic measurements is presented by using a Nearest Euclidean distant point definition. These geomagnetic approaches are then integrated to the

Inertial Navigation System to conform the Geomagnetic Aided Navigation mathematical model architecture. Additionally, the development of a simulation environment shown at the end of the chapter along with the designed Simulink blocks. This model is proposed to evaluate the performance of the algorithms in proposed conditions. Last, a physical set up of a quadcopter model it is presented aiming for experimental measurements and assessment of effects due to external factors.

Chapter 4 presents the results generated from the study of the algorithms presented in Chapter 3, in the scenarios proposed using the simulation environment. Specifically, two trajectories are defined and assessments of the accuracy of the estimations methods are given by analysing each independent methodology up to the integration of the full Geomagnetic aided navigation architecture. This includes, INS, INS-GMA, INS-EKF, and GAN with and without GPS, and the influence of velocity measurement in the estimations. On the other hand, the chapter closes by analysing sources of noise detected from measurements obtained from experimental flights.

Lastly, the Conclusion section closes the document with a summary of the information presented in the preceding sections and outlines the author's evaluation of the results provided in this study supplemented by performance metrics and analysis of the data obtained from simulations, along with the experimental data. Optional views of continued investigation are presented based on the results.

## 2. Background

This chapter introduces the mathematical methods and physical phenomena involved in developing the Geomagnetic Aided Navigation (GAN) algorithm to help explain more complex correlations between them required to develop this work.

### 2.1. Earth's Magnetic Field

As the Earth rotates, electric currents are generated due to molten iron and nickel movement around the outer core. This phenomenon is caused by heat escaping from the core, causing convection currents. The Earth's magnetic field is commonly shown as a dipole tilted 11 degrees related to its rotation axis, as shown in Figure 2.1. When using a compass, these devices will point to the magnetic north instead of the geographical north. These magnetic poles are not stationary and rotate around the geographic pole every 2000 to 3000 years (Goldenber 2006; Storms, 2009).

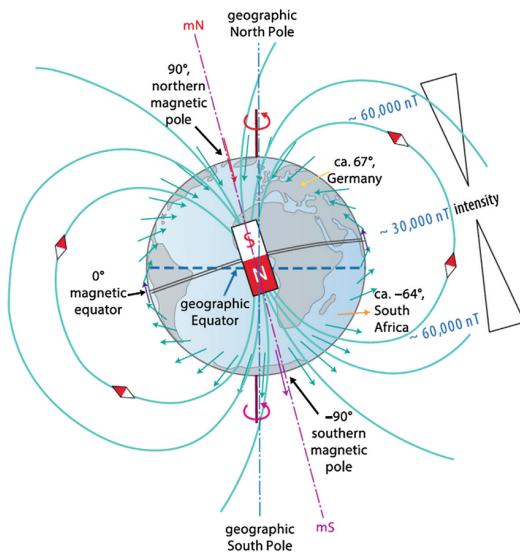


*Figure 2.1* Dipole Representation of earth's Magnetic field with its magnetic and true North (Balay, 2018).

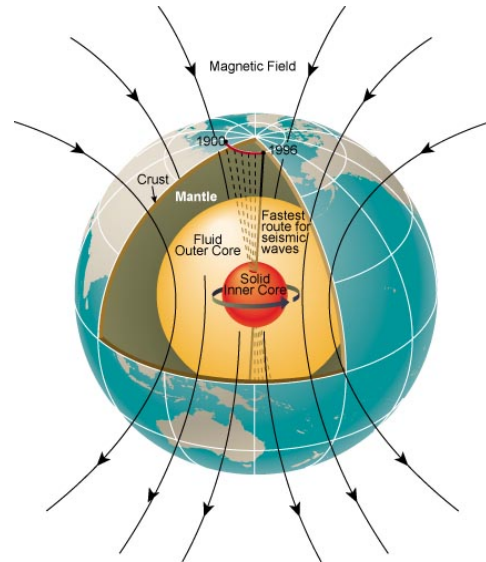


*Figure 2.2* Earth's core with its Magnetic flux lines (Lang, 2010).

In addition to external factors, small variations can be found, and rock concentrations underground known as Crustal rocks also contribute to local variations in the magnetic field. These variations are stronger closer to the Earth's surface.

As a practical approach, the total magnitude of the Earth magnetic field can be decomposed into three main components, the Main Field Component  $H_M$  emanating from the outer core fluid, the crustal anomalies component  $H_A$  from magnetized crustal rock underneath the surface, and magnetic disturbances  $H_d$  as currents flowing in the ionosphere and magnetosphere (Y. Liu et al., 2008). The total magnetic field can be represented as:

$$H_T = H_M + H_A + H_d \quad (2.1)$$

The main component covers more than 95% of the total magnitude while the component due to the anomalies rounds 4% of the sum. The remaining 1% comes from disturbances including diurnal variations. This magnitude became an interesting source of information because it has a unique characteristic. It can be described as a vector, with a direction and magnitude and it can be decomposed along different axis as shown in the Figure 2.3. Generally, the magnetic field vector is resolved under three components along of coordinate axis NED: Geographical North, East and Downward direction perpendicular to the surface. The projection of the Magnetic field vector into the horizontal plane, called horizontal component, always points to the geomagnetic north. The angle between the horizontal component and the geographical North is called magnetic declination. The angle between the magnetic vector  $H_T$  and the horizontal plane is the magnetic inclination (Y. Zhang et al., 2020).

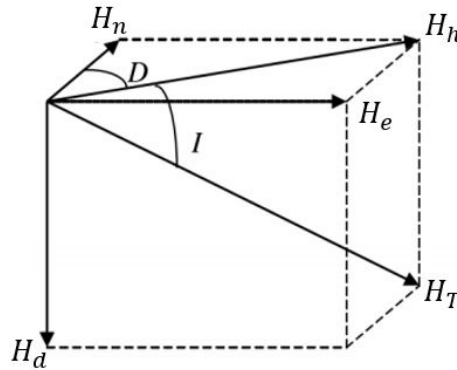


Figure 2.3 Earth's Magnetic field vector Decomposition.

Currently, the National Oceanic and Atmospheric Administration (NOAA) has information related to all of the geomagnetic elements presented in Figure 2.3. Since the data is collected through satellite measurements, it is important to recognize that the magnetic models presented by NOAA characterizes the main field component  $H_M$ . This means that a magnetic sensor or compass may observe spatial and temporal magnetic anomalies due to the other components.

## 2.2. Coordinate Transformation

Navigation often refers to the localization of systems over a specified referential frame. A reference frame is defined as a coordinate system to which measurements and estimations are referred to, so localization is related to a position in a frame.

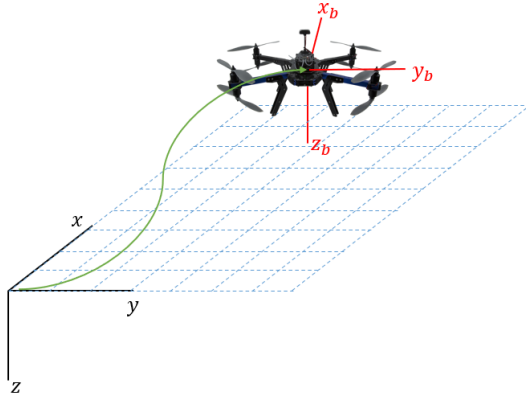


Figure 2.4 Inertial and body reference Frames

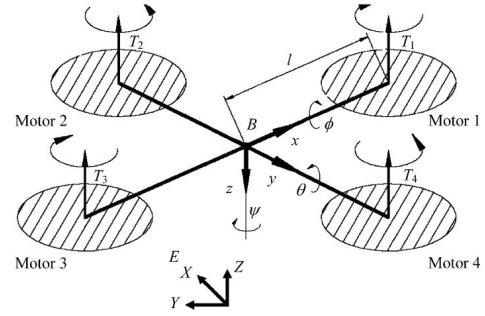


Figure 2.5 Forces and moments acting in a quadrotor (Mian & Daobo, 2008)

In aviation, two coordinate or axis frames are commonly defined, one as a point reference frame and the other is attached to the body, called body frame, as shown in the Figure 2.4. The vehicle's absolute position is defined in the inertial reference frame as  $x, y, z$ , and the orientation of the vehicle is defined by the Euler Angles  $\phi, \theta, \psi$ , while the angular velocities  $p, q, r$ , and body linear velocities  $V_Bx, V_By, V_Bz$  are defined in the body reference frame. To express the information from one frame into the other, a transformation is needed, which is known as coordinate transformation. The orientation of the vehicle can be described by three sequential rotations, whose order is important. Since the initial frame

is set as North, East, Down (NED), these rotations from the inertial frame to the body frame can be defined as:

$$R(x, \phi) = \begin{bmatrix} 1 & 0 & 0 \\ 0 & \cos(\phi) & \sin(\phi) \\ 0 & -\sin(\phi) & \cos(\phi) \end{bmatrix} \quad (2.2)$$

$$R(y, \theta) = \begin{bmatrix} \cos(\theta) & 0 & -\sin(\theta) \\ 0 & 1 & 0 \\ \sin(\theta) & 0 & \cos(\theta) \end{bmatrix} \quad (2.3)$$

$$R(z, \psi) = \begin{bmatrix} \cos(\psi) & \sin(\psi) & 0 \\ -\sin(\psi) & \cos(\psi) & 0 \\ 0 & 0 & 1 \end{bmatrix} \quad (2.4)$$

The product of the Matrices (2.2), (2.3), (2.4) in the given order results in the rotation matrix  $R$  shown in Equation (2.5), which relates a point in the inertial frame onto the body frame in terms of the Euler angles (Nelson et al., 1998).

$$R_I^B(\phi, \theta, \psi) = \begin{bmatrix} C_\theta C_\psi & C_\theta S_\psi & -S_\theta \\ S_\phi S_\theta C_\psi - C_\phi C_\psi & S_\phi S_\theta S_\psi + C_\phi C_\psi & C_\theta S_\phi \\ C_\phi S_\theta C_\psi + S_\phi S_\psi & C_\phi S_\theta S_\psi - S_\phi C_\theta & C_\theta C_\phi \end{bmatrix} \quad (2.5)$$

If a transformation of linear positions, velocities or accelerations is required from the body frame to the inertial frame, it is just necessary to use the transpose of the rotation matrix, that is  $R^T$ . In this manner, any measurement or data seen from the Body reference frame can be translated to the Inertial reference frame for its interpretation. However, for the case of angular velocities and accelerations, it is not that intuitive as expected since the relation between the Euler rates and the angular rates is defined in between of rotations as follows:



$$\begin{bmatrix} p \\ q \\ r \end{bmatrix} = \begin{bmatrix} \dot{\phi} \\ 0 \\ 0 \end{bmatrix} + R(x, \phi) \begin{bmatrix} 0 \\ \dot{\theta} \\ 0 \end{bmatrix} + R(x, \phi)R(y, \theta) \begin{bmatrix} 0 \\ 0 \\ \dot{\psi} \end{bmatrix} \quad (2.6)$$

The Equation (2.6) can be solved to find the relation between the Body angular velocities and the Euler rates as:

$$\begin{bmatrix} p \\ q \\ r \end{bmatrix} = \begin{bmatrix} 0 & 1 & -\sin(\theta) \\ 0 & \cos(\phi) & \sin(\phi)\cos(\theta) \\ 0 & -\sin(\phi) & \cos(\phi)\cos(\theta) \end{bmatrix} \begin{bmatrix} \dot{\phi} \\ \dot{\theta} \\ \dot{\psi} \end{bmatrix} \quad (2.7)$$

### 2.3. Equations of Motion

The rigid body equations of motion are obtained from Newton's second law that correlates the external forces existing on a body with the body's change of linear and angular momentum. It is possible to demonstrate that the moments  $M_x, M_y, M_z$  and Forces  $F_x, F_y, F_z$  can be written as shown in equations (2.8) and (2.9), where  $I_x, I_y, I_z$  refers to the moments of inertia and  $I_{xz}, I_{zy}, I_{yz}$  are the products of inertia. For a detailed development of these equations refer to the Book (Nelson et al., 1998).

$$\begin{aligned} M_x &= I_x \dot{p} - I_{zx} \dot{r} + qr(I_z - I_y) - I_{xz}pq \\ M_y &= I_y \dot{q} + rq(I_x - I_z) + I_{xz}(p^2 - r^2) \end{aligned} \quad (2.8)$$

$$\begin{aligned} M_z &= -I_{xz} \dot{p} + I_z \dot{r} + pq(I_y - I_x) + I_{xz}qr \\ F_x &= m(\dot{u} + qw - rv) + mg\sin(\theta) \\ F_y &= m(\dot{v} + ru - pw) - mg\cos(\theta)\sin(\phi) \\ F_z &= m(\dot{w} + pv - qu) + mg\cos(\theta)\cos(\phi) \end{aligned} \quad (2.9)$$

### 2.3.1. Vehicle's Dynamical Model

The platform selected to develop and test the algorithms was a quadcopter since it allows to perform steady and slow flights thanks to its ability to hover. It is necessary to understand the dynamics involved to construct a simulation environment that can provide clues in the algorithm development. Starting from the Equations (2.8) and (2.9), the next step is to characterize the forces and moments involved in the quadcopters dynamics. The absolute position is defined in the inertial frame as  $[X, Y, Z]$  while the angular position is defined by the euler angles  $[\phi, \theta, \psi]$ . The forces and moments acting on the vehicle are described in the Figure 2.5, and can be written as presented in Equations (2.10).

$$\begin{bmatrix} Mx \\ My \\ Mz \\ Fz \end{bmatrix} = \begin{bmatrix} Kl(w_4^2 - w_2^2) \\ Kl(w_3^2 - w_1^2) \\ b(w_4^2 - w_3^2 + w_2^2 - w_1^2) \\ T_1 + T_2 + T_3 + T_4 \end{bmatrix} \quad (2.10)$$

For the quadcopter model, it is assumed a symmetric geometry which cancels the product of inertia components of the Inertia tensor. By applying this concept and replacing Equation (2.10) into Equations (2.8), the actuators can be included in the equations of motion described by the motor velocities  $w_1, w_2, w_3$  and  $w_4$ .

$$\begin{aligned} Kl(w_4^2 - w_2^2) &= I_x \dot{p} + qr(I_z - I_y) \\ Kl(w_3^2 - w_1^2) &= I_y \dot{q} + rp(I_x - I_z) \\ b(w_4^2 - w_3^2 + w_2^2 - w_1^2) &= I_z \dot{r} + pq(I_y - I_x) \end{aligned} \quad (2.11)$$

Since all the forces from the motors point towards the Z axis in the body frame, the forces acting in Fx and Fy are zero. Finally, the state vector that describes the vehicle dynamics can be expressed as  $\vec{x} = [X, Y, Z, V_x, V_y, V_z, \phi, \theta, \psi]$ .

## 2.4. Inertial Navigation System

An INS is a combination of tools that can provide continuous and real-time navigation information to the carrier. This system relies on the inertial properties of sensors mounted onboard to execute the navigation function by appropriately processing the data obtained from accelerations and inertial angular velocity measurements (Britting, 1971). The vast majority of these systems contain the same major components, but differ in the accuracy that they can provide, and how fast it deviates from the original position. Commonly, INS components are resumed into accelerometers, gyroscopes and in some cases GPS, usually contained in Inertial Measurement Units (Storms, 2009).

The measurements obtained directly from an IMU do not give any information about the vehicle's current position. Hence, Aiding techniques are required to process all the information and obtain position estimation. Currently, the Kalman Filter (KF) is a famous and robust sensor fusion tool that perfectly fits applications that do not have demanding requirements. On the other hand, when problems with more complexity are given, it is possible to find variations of this technique as the Extended Kalman Filter (EFK), Unscented Kalman filter (UKF), Particle filter (PF), and others that are not limited to Bayesian estimators.

### 2.4.1. Bayesian Processing

The Bayesian estimation works around the probabilistic characteristic that comes with the action of measuring. When discussing probabilities, some of the terms that arise with this concept are the mean, standard deviation, density function, and samples. The Bayesian estimation objective is to find the most likely value starting from the system's actual state, the measurement taken, and the understanding of the vehicle's behavior from its dynamical model. Estimators based on the a posteriori density are usually called bayesian because they are deducted from the Bayes' theorem. The Bayes rule is defined as (Candy, 2016):

$$P(X|Y) = P(Y|X) \frac{P(X)}{P(Y)} \quad (2.12)$$

Bayes rule gives the probability that an hypothesis X is true given an event Y ( $P(X|Y)$ ), from how probable was the hypothesis X true before the event Y ( $P(X)$ ), how probable is the event Y given that the hypothesis X is actually true ( $P(Y|X)$ ), and how probable is the event Y by itself ( $P(Y)$ ).

Often, a system is described by a discrete stochastic model in the form:

$$\begin{aligned}x_k &= f_{k-1}(x_{k-1}) + v_{k-1} \\z_k &= h_k(x_k) + w_k\end{aligned}\tag{2.13}$$

where  $f_{k-1}$  represents the state transition model,  $v$  is the noise that describes unforeseen disturbances in the motion,  $Z_k$  is the measurement and  $h_k$  is the measurement equation.

#### 2.4.2. Kalman Filtering

The Kalman filter is an optimal algorithm derived from Bayes' theorem that assumes the posterior density as Gaussian and hence characterized by a mean and covariance. Additionally, the state and measurement transition models  $f_{k-1}$  and  $h_k$  are assumed to be linear functions. When a new measurement is available, the update of the probability density function (PDF) is calculated by rewriting Equation (2.12) as:

$$P(x_k|Z_k) = \frac{P(z_k|x_k)P(x_k|Z_{k-1})}{P(z_k|Z_{k-1})}\tag{2.14}$$

The PDF function of a Gaussian distribution is a characteristic symmetric "bell curve" shape as shown in Figure 2.6, and it is described by the following Equation (Gordon et al., 2004):

$$P(x; \mu, \sigma) = \sqrt{(2\pi\sigma)} e^{-\frac{1}{2}(\frac{x-\mu}{\sigma})^2}\tag{2.15}$$

where  $\mu$  is the mean and  $\sigma$  the standard deviation.

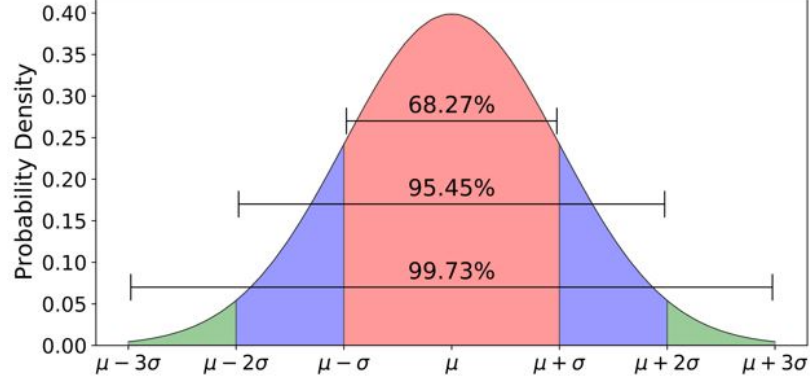


Figure 2.6 Gaussian Normal distribution and its probability regions (Galarnyk, 2019)

The equations that describe the Kalman Filter process to estimate a given state, including the appropriate mean and covariance update are (Gordon et al., 2004):

$$\hat{x}_{k|k-1} = F_{k-1}\hat{x}_{k-1|k-1} \quad (2.16)$$

$$P_{k|k-1} = Q_{k-1} + F_{k-1}P_{k-1|k-1}F_{k-1}^T \quad (2.17)$$

$$\hat{x}_{k|k} = \hat{x}_{k|k-1} + K_k(z_k - H_k\hat{x}_{k|k-1}) \quad (2.18)$$

$$P_{k|k} = P_{k|k-1} - K_k S_k K_k^T \quad (2.19)$$

$$S_k = H_k P_{k|k-1} H_k^T + R_k \quad (2.20)$$

The KF computes the mean and the covariance of the Gaussian posterior  $P(x_k|Z_k)$  iteratively represented by the state  $\hat{x}$  and P respectively.  $K_k$  is known as the Kalman gain, Q and R are the process and measurement noise covariances, while F and H are the state transition and observation matrices. The Kalman filter is performed in two steps, the state prediction and the measurement update, each denoted by the subindex  $k|k-1$  and  $k$  respectively. The solution of the KF is the optimal solution for a linear gaussian problem while the postulates made are hold. The estimated state resulting from the KF will be the most likely value according to the new posterior density function assessed.

### 2.4.3. Extended Kalman Filtering

The main concern about the KF is that it only works for linear systems, and by default, most problems in nature manifest itself as complex with non-linear behaviors. Therefore, variations of the KF as the Extended Kalman Filter exist to deal with some non-linear cases. The main feature in the EKF is that it linearizes the non-linear function of the state dynamics and measurement models.

Similarly, as the KF, the EKF starts from the same model presented in Equation (2.13). The random white Gaussian noises described with  $v_{k-1}$  and  $w_k$  are mutually independent, zero-mean with covariances  $Q_{k-1}$  and  $R_k$  respectively. Now it is assumed that equations (2.13) are non-linear; these are approximated by the first term in their Taylor Series expansion, which results being the Jacobian, and will be denoted as  $\hat{F}$  and  $\hat{H}$ . This assumes that that local linearization may be enough characterization of the nonlinearity (Gordon et al., 2004). The new equations for EKF are defined as follows:

$$\hat{x}_{k|k-1} = f_{k-1}(\hat{x}_{k-1|k-1}) \quad (2.21)$$

$$P_{k|k-1} = Q_{k-1} + \hat{F}_{k-1} P_{k-1|k-1} \hat{F}_{k-1}^T \quad (2.22)$$

$$\hat{x}_{k|k} = \hat{x}_{k|k-1} + K_k(z_k - h_k(\hat{x}_{k|k-1})) \quad (2.23)$$

$$P_{k|k} = P_{k|k-1} - K_k S_k K_k^T \quad (2.24)$$

$$S_k = \hat{H}_k P_{k|k-1} \hat{H}_k^T + R_k \quad (2.25)$$

The EKF and further variations of the KF are referred as analytic approximations because the linearizations are calculated analytically. On the other hand, estimations based on points are refereed as deterministic since their approach are based on evaluation of Batches of particles. These concepts will be used to build the main Inertial Navigation system described in this thesis.

## 2.5. Geomagnetic Aided Navigation

Geomagnetic Aided Navigation, or GAN, uses the magnetic elements presented in Figure 2.3, for navigation purposes. This idea was first proposed decades ago and it has not been used by humans, but also, there are scientific reports (Johnsen et al., 2020) that show proof of animals able to use the magnetic field as a way to guide themselves through the ocean, able to travel long distances and return home.

As shown in Chapter 1, the idea of geomagnetic navigation is similar to the concept of terrain navigation, and one possible way to define it is as a contour matching problem, where an identified map exists, and correlational measurements are available through all time. Different papers have been published up to date (Duan et al., 2019; Luo et al., 2008; M. Liu et al., 2014; Nygren, 2008; Turan & Kutay, 2016; Zhao et al., 2014), working around this problem. Most of this publications focuses in two main areas, The first is to improve the accuracy of the Matching algorithms also based on contour matching as for example in (Duan et al., 2019) and (Xiao et al., 2020), where probabilistic considerations are taken in the sensor data before a contour matching. Here it is proposed to regenerate the measurements based on the probabilistic parameters from the sensor. Secondly, it is study the improvement of the estimations with the data from the Geomagnetic matching by using error models, particle filters, kinematic constraints or artificial intelligence.

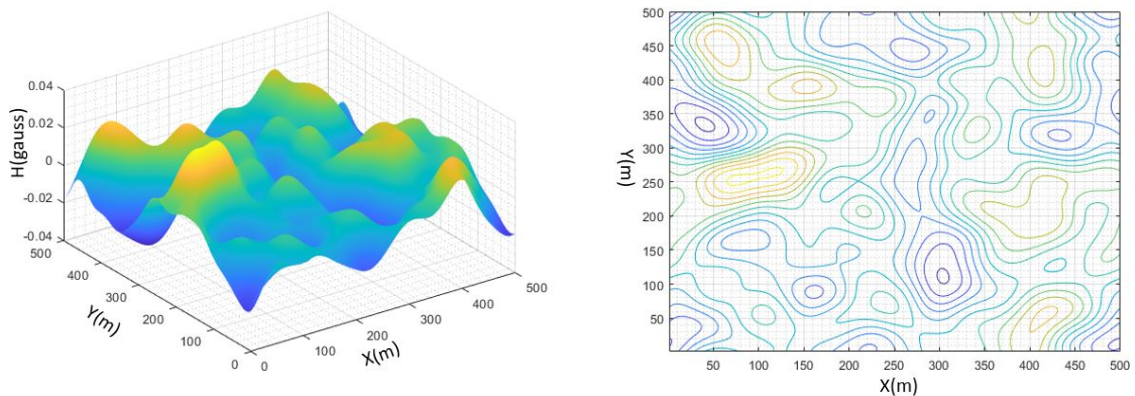


Figure 2.7 Example of Geomagnetic Map and its corresponding contour lines

The type of maps and contours that characterize the magnitude of the Earth's magnetic field is similar to those displayed in Figure 2.7, 2.9 and 2.10. Therefore, any random measurement can be correlated to the contour information of the map. A position estimated from an INS can be corrected by correlating the magnetic measurements with the known contours by finding the possible best fit in the magnetic surface, as presented in the Figure 2.8 (Duan et al., 2019). Here, the real positions at every sample time of the trajectory  $M_1, M_2, \dots, M_5$  have an associated magnetic value that characterises a contour line. Then the INS estimations  $I_1, I_2, \dots, I_5$  are corrected to the closest position  $N_1, N_2, \dots, N_5$  that matches the same contour line as the measurement. This process is known as contour matching and it has been focus of various investigations since the projects TERCOM and MAGNET, and last decade (Duan et al., 2019; M. Liu et al., 2014; Lin et al., n.d.).

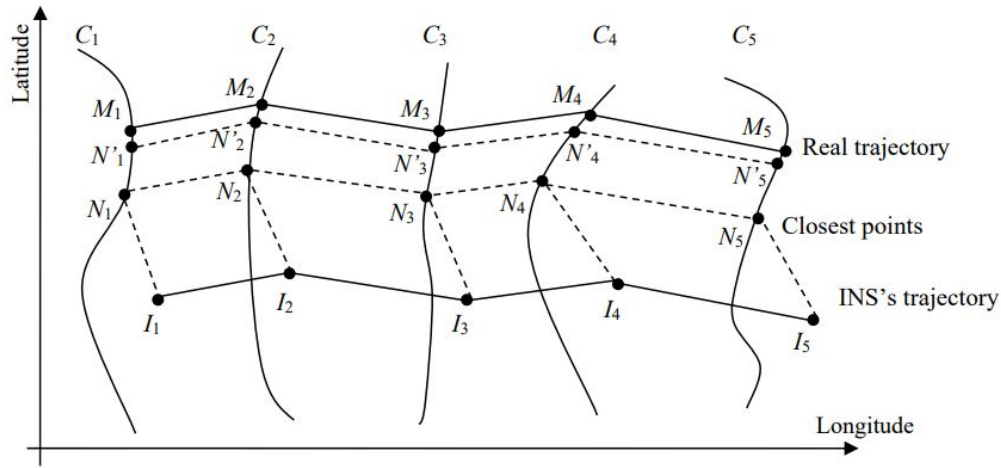


Figure 2.8 Example of contour matching. Image extracted from (Duan et al., 2019)

Diverse scenarios have been identified within the literature review of this concept and have been separated into three categories for outdoor navigation, where the approach of the problem requires a variation of the tools needed and the resolution it may provide.

### 2.5.1. High Altitude Navigation

Considering altitudes up to 15km, the Earth's Magnetic field curvature can be neglected, and the magnetic field is considered as a combination of the Main field and the Crustal field.



As the Magnetic field is measured far from the surface, the crustal rocks' component will become null, and the observation will be mainly composed of the Main field. Therefore, the World Magnetic model provided by the NOAA can be used as a map reference source. The types of map available suggest that missions requiring high accuracy estimation may not be eligible for this category. Figure 2.9 exposes one of the maps available at NOAA database (Oceanic & Administration, n.d.). NOAA provided different maps characterizing the elements presented in the Figure 2.3.

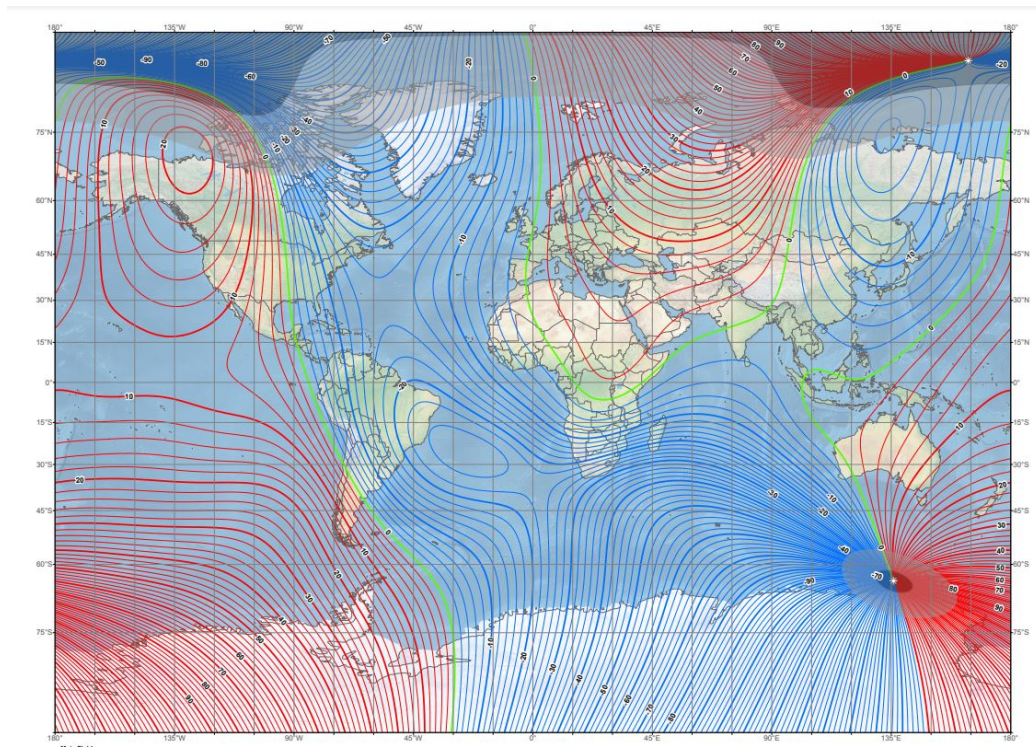


*Figure 2.9 Declination Map available at NOAA (Oceanic & Administration, n.d.).*

### **2.5.2. Low Altitude - High Range**

Below 15km altitudes, the magnetic anomalies due to concentrated crustal rocks produce detectable features in the Earth's magnetic field. These features have been measured over the years including the project Magnet, up to nowadays with modern satellites. Thanks to this effort more than 95% of Earth's cortex have been identified and the data is published for its use.

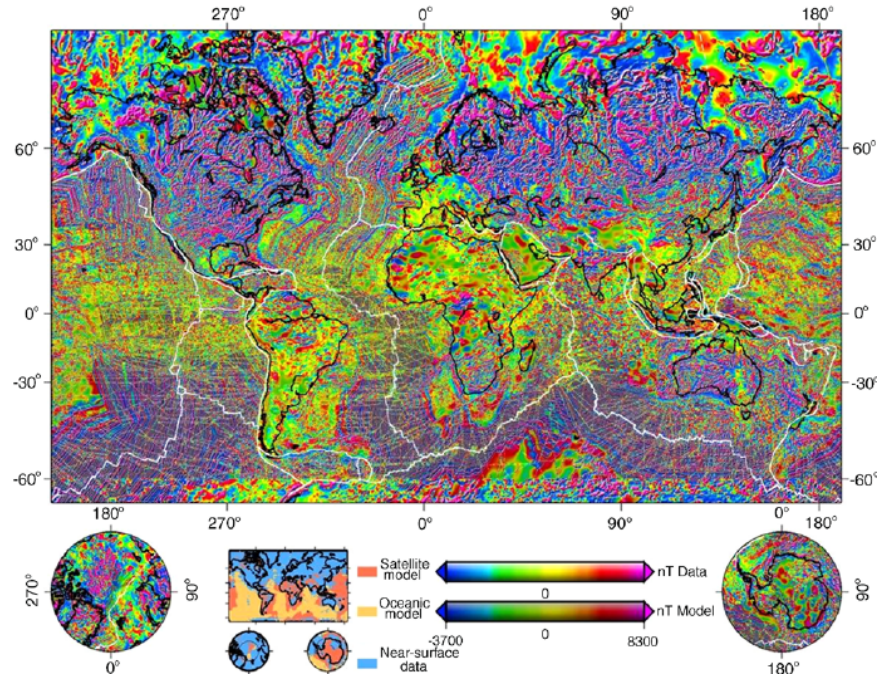


*Figure 2.10* World Anomaly Magnetic Map (Oceanic & Administration, n.d.).

The Figure 2.10 plots the database available in Official US government websites as NOAA (Oceanic & Administration, n.d.), characterizing the anomaly magnetic field. This information can be used as map source for long range applications at low altitudes. The magnetic anomaly map is specified as a global 3-arc-minute, meaning that for application that require better resolutions, specific or localized maps have to be built.

### **2.5.3. Low Altitude - Low Range**

Low altitude, low range are the scenarios that require more accurate maps with higher resolution since it can not be provided by the anomaly map. This research project proposes the measurement of the field at a local area by constructing the grid experimentally. These problems could be consider similar to research efforts that aims to characterize indoors areas for navigation's. An important difference between this scenarios is that indoors areas have multiple magnetic sources as power plants, ferromagnetic structures, cables etc. These sources can be used as local references, facilitating the navigation process. One example is presented in (Storms, 2009) as shown in figure 2.11, where the magnetic components of the field of a hallway are measured.

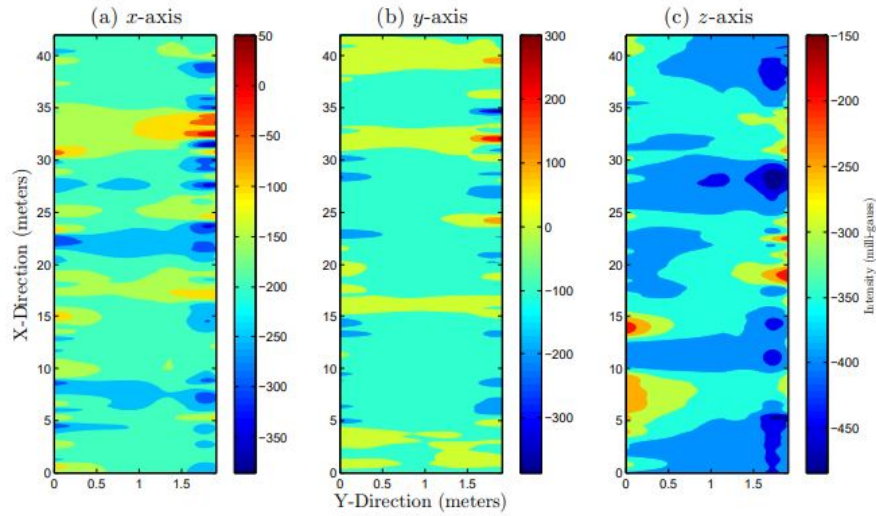


*Figure 2.11* Fingerprints of the Magnetic components measures in (Storms, 2009)

Additionally, for outdoors scenarios, often sensors are attached to planes as in (Goldenber, 2006) and other modern experiments. This requires an intense effort since more resolution translates to more data points, and increased costs for extended areas. This approach may not be suitable for all regions understanding the complexity or restrictive access to some objective fields.



### 3. Methodology

This chapter describes the development of the Geomagnetic Aided Navigation algorithm as proposed in the architecture shown in Figure 3.1. This scheme is composed by several interconnected sub algorithms that compose the full navigation method, starting with the magnetic database, a geomagnetic matching method, a geomagnetic positioning algorithm, and the INS as basis of the GAN structure.

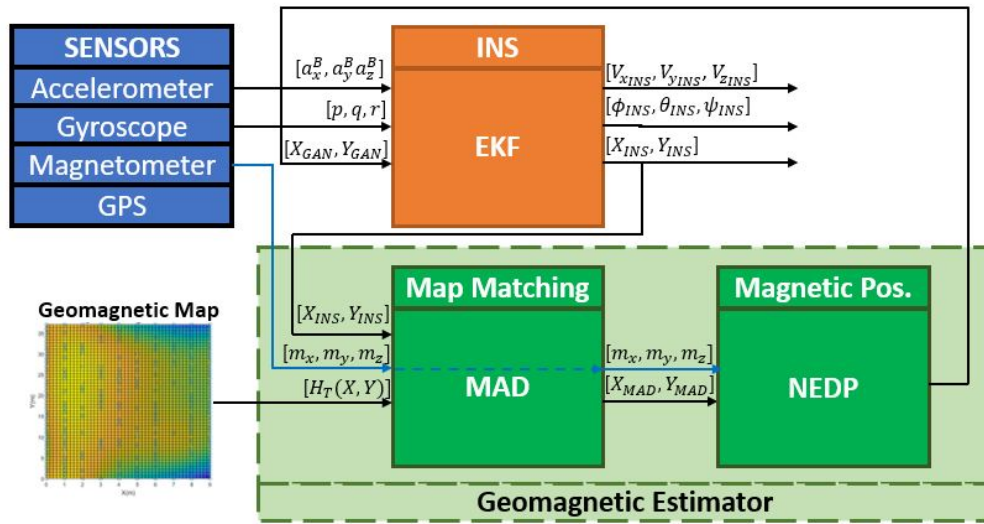


Figure 3.1 Geomagnetic Aided Navigation schematic proposed

Lastly, a simulation environment was developed to perform numerical simulations and assess the capabilities and performance of the GAN algorithm and each of its sub algorithms.

#### 3.1. Geomagnetic Map and Database Generation

The GAN algorithm heavily relies on the existence of a magnetic map of the area of interest since it is the core of the correlation process. The scenario proposed is outdoors: short range-low altitude, where the algorithm will work around measurable variations of the Crustal Magnetic field. The area selected for the geomagnetic measurement was a section of the Embry-Riddle Aeronautical University Softball Turf field, presented in Figure 3.2.



Figure 3.2 Testing Area at ERAU outdoor facility

c



Figure 3.3 Microstrain 3DM-GX4-45 Sensor

Prior to measuring the Magnetic field, the sensor was calibrated to compensate for possible environmental noise and manufacturing defects. Absent any magnetic interference, magnetometer readings will measure only the Earth's magnetic field. If magnetometer measurements are taken as the sensor is rotated through all possible orientations, the measurements should lie on a sphere. The radius of the sphere is the magnetic field strength(Kok & Schön, 2016). The calibration method corresponds to the translation  $b_{offset}$  and scaling  $A_{scaling}$  of the raw ellipsoid  $H$  conformed by the data into the calibrated sphere

$H_{calibrated}$ . By collecting different points, a calibration process can be seen as shown in Figure 3.4.

$$H_{calibrated} = A_{scaling}(H_{vector} - b_{offset}) \quad (3.1)$$

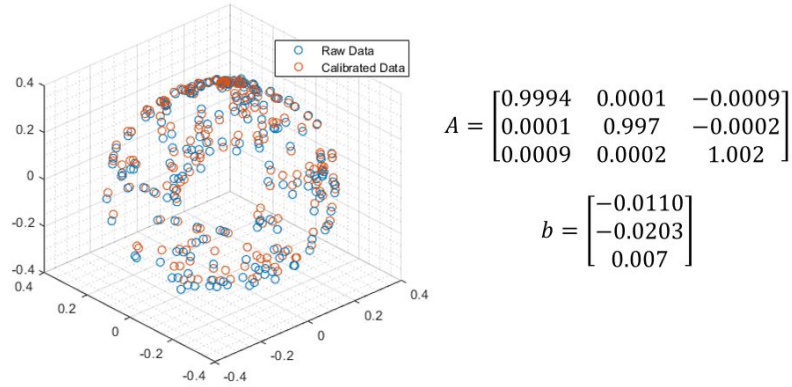


Figure 3.4 Sensor raw data and Calibrated Data

Table 3.1

Microstrain Magnetometer Sensor specifications

Parameter	Value
Noise Density	$100\sqrt{Hz}$
Measurement range	+/- 2.5Gauss
Initial Bias error	+/-0.003 Gauss
Alignment Error	0.05 Degrees

After the map of the Magnetic field's magnitude is constructed as shown in Figure 3.5, a linear interpolation can be performed in between each measurement to generate a more refined dataset to be stored and used in the GAN algorithm. This new interpolated dataset has a resolution of 10cm, instead of 1m, resulting in a map of 91 by 371 points.

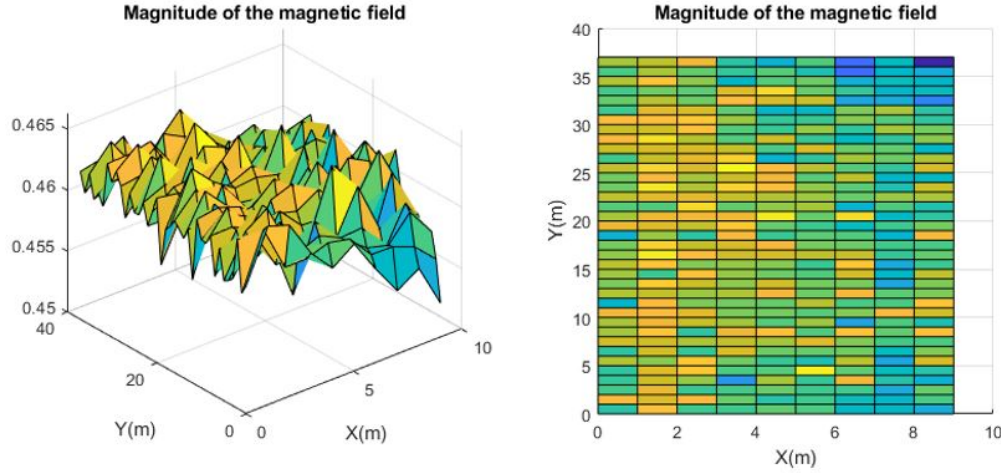


Figure 3.5 Measured Magnetic Field's Magnitude map at Embry-Riddle Softball field

At last, for testing purposes with the objective of evaluating differences in the response of the GAN algorithm, the data measured was approximated to different polynomial surfaces varying from 2th to 5th order searching for the surface that best fits the cloud of points. This approximation gives a smoother surface and can be used as a magnetic true model in the simulated environment, based on the real data. The best fit from the polynomial approximation is chosen by evaluating a goodness-of-fit tool called reduced Chi-squared statistic defined by:

$$\chi_v^2 = \frac{1}{v} \sum_{i=1}^{381 \times 91} \left( \frac{H_m(i) - H_{Fit}(i)}{\sigma_m^2} \right) \quad (3.2)$$

where  $H_m(i)$  is the magnetic measurement and  $H_{Fit}(i)$  is the fit value at the given position,  $v$  is the degree of freedom (defined by the number of points evaluated in the fit minus the parameters being estimated in the fit), and  $\sigma_m$  is the uncertainty of the measurement defined by the standard deviation of its noise calculated from the noise density presented in Table 3.1 at 50Hz. Once calculated the reduced Chi squared value, if  $\chi_v^2 \gg 1$ , it indicates a poor model fit. A  $\chi_v^2 > 1$  indicates that the fit has not fully captured the data, and if it is close to 1 the fit goes in concordance with error variance. For  $\chi_v^2 < 1$  the model is over fitting the data (Bevington et al., 1993).

Once defined the map and a refined grid, the Geomagnetic Matching is the first step to construct a GAN algorithm, and normally it is used to correct the drift produced by the error integration from in the INS. The Matching process correlates the INS path profiles with the map discussed in section 3.1 by analyzing a small area of the map at the surroundings of the INS estimation. This area is denominated as the uncertainty Area.

### 3.1.1. Uncertainty Area

Traditional Matching methods have two main characteristics, searching strategy, and correlation length. The searching strategy is carried inside and uncertainty area  $U$ , normally defined by the INS's uncertainty. This means its standard deviation when referring to Gaussian distributions. This brings up the first drawback that this type of method has: the bigger the data set to be compared, the less computationally efficient the matching will become. As defined in Equation (3.3), a good rule of thumb is to define an area of maximum  $+/- 3\sigma$  around the INS point since a  $3\sigma$  represents the boundaries where 99.73% of the probabilities will rely, as shown in Figure 2.6.

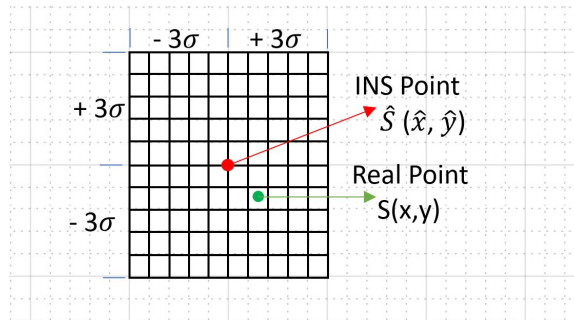


Figure 3.6 Uncertainty Area boundaries

Although the uncertainty area is defined by a circle with radius  $3\sigma$ , a square shape is selected due to computational adaptability. Additionally, it is possible to define the boundaries for the  $X$  and  $Y$  position independently if the independent covariances are available respectively.



$$U = [(x, y), |x - \hat{S}_x| \leq 3\sigma \ \& \ |y - \hat{S}_y| \leq 3\sigma] \quad (3.3)$$

When the vehicle starts navigating, magnetometers will start measuring at each time step ( $k$ ; 1,2,...,N) the Magnetic Field's Magnitude,  $H_m = [h_{m,1}, h_{m,2}, \dots, h_{m,N}]$ . Additionally, each value of  $H_m$  is associated with a position in space estimated by the INS that will be denoted as  $\hat{S}$ . Given this statement, there will be N position points that defines the whole trajectory  $\hat{S} = [\hat{S}_1, \hat{S}_2, \dots, \hat{S}_N]$ . Following the Equation (3.3), the uncertainty area can be described as Figure 3.6. For the purposes of this study, the area was chosen to be 1m by 1m with 11 by 11 points given in a grid resolution of 0.1m. However, it must be emphasized that the uncertainty area can be variable if independent covariances for the positions are available .

### 3.1.2. Correlation Analysis

Each point included in the Uncertainty Area in Figure 3.6, denoted as  $U(i, j)$  has a Magnetic value defined by the map described in Figure 3.5. The goal is to compare the measurement taken at the sample time  $i$  against all the Magnetic values assigned to each point in the area.

#### 3.1.2.1. Minimum Difference

An intuitive initial guess is to select the Magnetic value of the uncertainty area closest from the taken measurement at each iteration, as presented in Equation (3.4). However, intrinsically all measurement systems are affected by noise and external factors that can always may generate disturbances. This will induce additional noise in the correlation. For this reason, it is necessary to develop Equation (3.4) in a more robust expression based on correlation of prior measurements as Equation (3.5).

$$\min(CP(i, j)) = |H_{U(i,j),k} - H_{m,k}|, (i, j) \in U \quad (3.4)$$

### 3.1.2.2. Mean Absolute Deviation

In statistics, there exist four important correlation rules used in correlative analysis, the Product correlation (PROD), the normalized product correlation (NPROD), the Mean absolute deviation (MAD), and Mean variance algorithm (MSD) (Y. Liu et al., 2008) (Wei et al., 2011). The PROD and NPROD emphasize in the similarity between two sets while the MAD emphasize in the degree of difference between the sets. Although all options are widely used, the option selected for this study is the MAD algorithm based on references (Chang, 2017; Y. Liu et al., 2008), and it follows the mathematical expression shown in the Equation (3.5).

$$\min(MAD(i, j)) = \frac{1}{N} \sum_{k=1}^N |H_{U(i,j),k} - H_{m,k}|, (i, j) \in U \quad (3.5)$$

The Equation (3.5) is described for the full path, referring to all the sampled times of the mission, but it is necessary to mention that the longer the set of points are being evaluated, the higher the possible false certainty of the algorithm, so it will converge to a unique solution that may be not the correct one. On the other hand, if a short set of points is used, it will be prompt to jump constantly between guesses from the same reason as the closes point or minimum difference. Within this algorithm, it is assumed that there exist  $i * j$  parallel paths to be compared to the measured sequence  $H_m$ . The MAD algorithm tells the path in the uncertainty area that deviated the least from the measured sequence.

### 3.1.3. Geomagnetic Matching

The MAD algorithm is applied at each iteration as explained in Figures 3.7 to 3.10. The INS output is approximated to the closest position of the grid and the sequence of measurements  $H_{m,k}$  is compared to the sequence respective to each point inside the area  $U_k(i, j)$ . The path with the minimum mean deviation is then selected. When another path of the uncertainty area gets a minimum MAD correlation than the current path, the algorithm switches to the new position as shown in Figure 3.10.

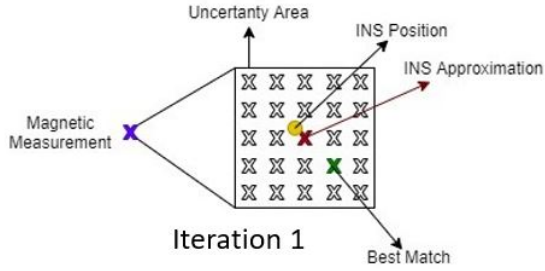


Figure 3.7 MAD iteration 1 - Set up of each point

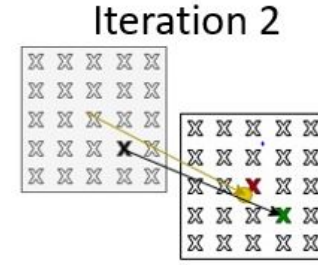


Figure 3.8 MAD iteration 2 - First match.

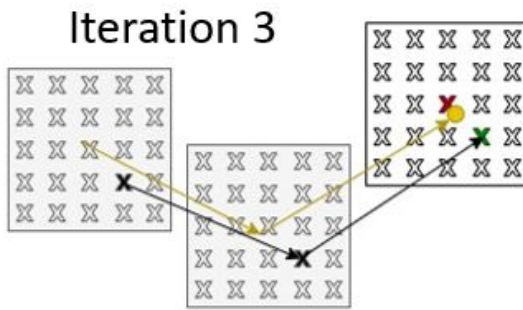


Figure 3.9 MAD iteration 3 - Second match at same path.

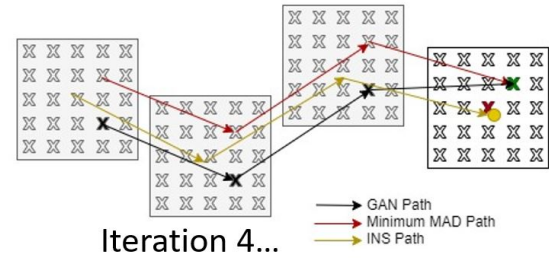


Figure 3.10 MAD iteration 4 - Second match at different path.

Once selected the point in the uncertainty area that best fits the history of magnetic measurements, a position in the geomagnetic map that matches the current measurement has to be found. Since there may exist multiple positions with the same magnetic values, it is required to define a method to select the correct one.

#### 3.1.4. Nearest Euclidean Distance Point

The nearest euclidean distance assigns the largest probability to the closest point of the map with the same magnetic value measured from the sensor, the Figure 3.11 shows an example of the approximation of the algorithm. In the implementation, the location of each point that matches the contour curve is compared to the location of the estimated position and the closest one will become the most probable estimation. This process is performed to increase the reliability on the geomagnetic estimation.

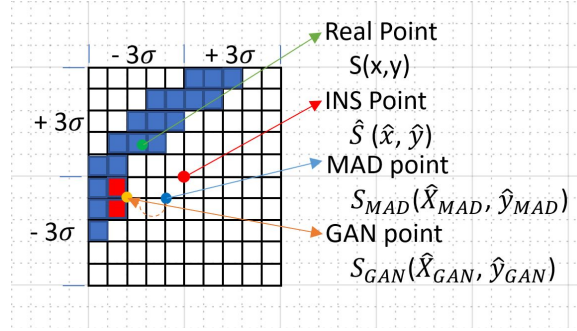


Figure 3.11 Representation of the Nearest Distance point

The NEDP can be calculated by evaluating the 2D distance of all the points in the uncertainty area against position given by the geomagnetic matching, this can be represented as follows:

$$\hat{X}_{NP} = \min(\sqrt{(\hat{X}_{GMA} - X_{H_{m,k}}(i, j))^2 + (\hat{Y}_{GMA} - Y_{H_{m,k}}(i, j))^2}) \quad (3.6)$$

### 3.2. Inertial Navigation System

To provide the initial point that defines the center of the uncertainty field, it is required to establish the Inertial Navigation System equations and define how the measured information obtained from the sensors is integrated. A strapdown inertial navigation System scheme can be defined as presented in the Figure 3.12, as follows:

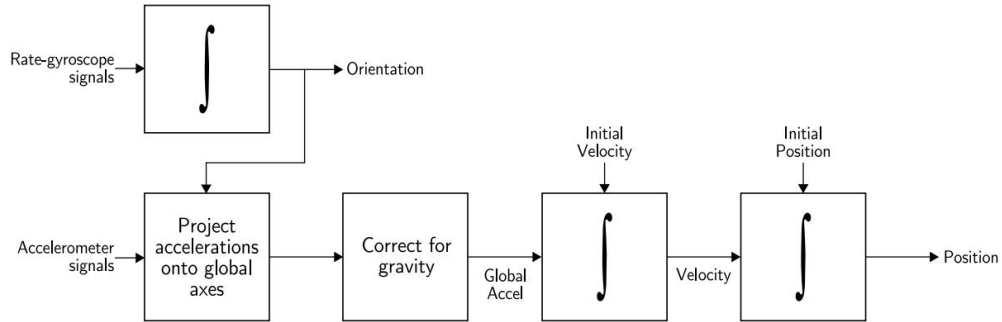


Figure 3.12 Strapdown Inertial Navigation System (Woodman, 2007).

Recalling the discrete definition of the systems states in Equation (2.13), the equations of motion presented on Chapter 2 and defining  $\hat{X}, \hat{Y}, \hat{Z}$  as the vehicle positions,  $\hat{V}_x, \hat{V}_y, \hat{V}_z$  as

velocities and  $\hat{\phi}, \hat{\theta}, \hat{\psi}$  as the Euler angles. Based on the scheme at Figure 3.12, the discrete non-linear model to be used as the base of the INS can be defined as follows:

$$\hat{X}_k = \hat{X}_{k-1} + \hat{V}_{x_{k-1}} \Delta t \quad (3.7)$$

$$\hat{Y}_k = \hat{Y}_{k-1} + \hat{V}_{y_{k-1}} \Delta t \quad (3.8)$$

$$\hat{Z}_k = \hat{Z}_{k-1} + \hat{V}_{z_{k-1}} \Delta t \quad (3.9)$$

$$\hat{V}_{x_k} = \hat{V}_{x_{k-1}} + a_x^I \Delta t \quad (3.10)$$

$$\hat{V}_{y_k} = \hat{V}_{y_{k-1}} + a_y^I \Delta t \quad (3.11)$$

$$\hat{V}_{z_k} = \hat{V}_{z_{k-1}} + a_z^I \Delta t \quad (3.12)$$

$$\hat{\phi}_k = \hat{\phi}_{k-1} + (p + q \sin(\hat{\phi}_{k-1}) \tan(\hat{\theta}_{k-1}) + r \cos(\hat{\phi}_{k-1}) \tan(\hat{\theta}_{k-1})) \Delta t \quad (3.13)$$

$$\hat{\theta}_k = \hat{\theta}_{k-1} + (q \cos(\hat{\phi}_{k-1}) - r \sin(\hat{\phi}_{k-1})) \Delta t \quad (3.14)$$

$$\hat{\psi}_k = \hat{\psi}_{k-1} + (q \sin(\hat{\phi}_{k-1}) \sec(\hat{\theta}_{k-1}) + r \cos(\hat{\phi}_{k-1}) \sec(\hat{\theta}_{k-1})) \Delta t \quad (3.15)$$

The Equations (3.7) to (3.15) correspond to the direct integration of each of the states given the sample time. It is important to note that Equations (3.10), (3.11), (3.12) require the accelerations in the Inertial body frame but only the accelerations at the body frame are measured. Therefore, the data from the accelerometers should be transformed from body to inertial frame using the rotation matrix (2.5) as shown in Equation (3.16). This architecture presents a problem when integrating the error in the estimation and generates a drift over time.

$$\begin{bmatrix} a_x^I \\ a_y^I \\ a_z^I \end{bmatrix} = \begin{bmatrix} C_\theta C_\psi & C_\theta S_\psi & -S_\theta \\ S_\phi S_\theta C_\psi - C_\phi C_\psi & S_\phi S_\theta S_\psi + C_\phi C_\psi & C_\theta S_\phi \\ C_\phi S_\theta C_\psi + S_\phi S_\psi & C_\phi S_\theta S_\psi - S_\phi C_\theta & C_\theta C_\phi \end{bmatrix}^T \begin{bmatrix} a_x^B \\ a_y^B \\ a_z^B \end{bmatrix} - \begin{bmatrix} 0 \\ 0 \\ g \end{bmatrix} \quad (3.16)$$

Finally, Equations (3.13), (3.14) and (3.15) are derived by solving the angular accelerations by inverting the Equations (2.7).

### 3.2.1. Inertial Measurement Unit

The IMU located at the center of mass, generally provides an array of 3-axis accelerometers, 3-axis gyroscopes and 3-axis magnetometers, represented by the notation  $a_x^B, a_y^B, a_z^B, p, q, r, m_x, m_y, m_z$  respectively. The accelerometer measures the Body frame acceleration, including the acceleration of the body plus the gravitational acceleration seen from this frame. The gyroscope measures the body angular velocities, and the magnetometer measures the magnetic field decomposed in the body frames axes. Additionally, a GPS can often be found capable of measuring positions and velocities in the inertial reference frame. This data is utilized in the Equations (3.7) to (3.15), and its integration is performed to complete the Inertial Navigation System. The GPS will come to use once the INS is enhanced with an Extended Kalman Filter.

### 3.3. Extended Kalman Filter

The EKF uses the Equations (3.7) to (3.15) into the Equation (2.21) for the State prediction. Due to the non-linearity of the equations, a linearization is required defining a linear transition model, also known as the Jacobian, and denoted by  $\hat{F}_{k-1}^T$ . This Jacobian is used in Equation (2.22), and given the 9 states of the system, the size of this matrix will be size 9 by 9 as follows:

$$\hat{F}_{k-1}^T = \begin{bmatrix} \frac{\partial X}{\partial X} & \frac{\partial X}{\partial Y} & \frac{\partial X}{\partial Z} & \frac{\partial X}{\partial V_x} & \frac{\partial X}{\partial V_y} & \frac{\partial X}{\partial V_z} & \frac{\partial X}{\partial \phi} & \frac{\partial X}{\partial \theta} & \frac{\partial X}{\partial \psi} \\ \frac{\partial Y}{\partial X} & \frac{\partial Y}{\partial Y} & \frac{\partial Y}{\partial Z} & \frac{\partial Y}{\partial V_x} & \frac{\partial Y}{\partial V_y} & \frac{\partial Y}{\partial V_z} & \frac{\partial Y}{\partial \phi} & \frac{\partial Y}{\partial \theta} & \frac{\partial Y}{\partial \psi} \\ \frac{\partial Z}{\partial X} & \frac{\partial Z}{\partial Y} & \frac{\partial Z}{\partial Z} & \frac{\partial Z}{\partial V_x} & \frac{\partial Z}{\partial V_y} & \frac{\partial Z}{\partial V_z} & \frac{\partial Z}{\partial \phi} & \frac{\partial Z}{\partial \theta} & \frac{\partial Z}{\partial \psi} \\ \frac{\partial V_x}{\partial X} & \frac{\partial V_x}{\partial Y} & \frac{\partial V_x}{\partial Z} & \frac{\partial V_x}{\partial V_x} & \frac{\partial V_x}{\partial V_y} & \frac{\partial V_x}{\partial V_z} & \frac{\partial V_x}{\partial \phi} & \frac{\partial V_x}{\partial \theta} & \frac{\partial V_x}{\partial \psi} \\ \frac{\partial V_y}{\partial X} & \frac{\partial V_y}{\partial Y} & \frac{\partial V_y}{\partial Z} & \frac{\partial V_y}{\partial V_x} & \frac{\partial V_y}{\partial V_y} & \frac{\partial V_y}{\partial V_z} & \frac{\partial V_y}{\partial \phi} & \frac{\partial V_y}{\partial \theta} & \frac{\partial V_y}{\partial \psi} \\ \frac{\partial V_z}{\partial X} & \frac{\partial V_z}{\partial Y} & \frac{\partial V_z}{\partial Z} & \frac{\partial V_z}{\partial V_x} & \frac{\partial V_z}{\partial V_y} & \frac{\partial V_z}{\partial V_z} & \frac{\partial V_z}{\partial \phi} & \frac{\partial V_z}{\partial \theta} & \frac{\partial V_z}{\partial \psi} \\ \frac{\partial \phi}{\partial X} & \frac{\partial \phi}{\partial Y} & \frac{\partial \phi}{\partial Z} & \frac{\partial \phi}{\partial V_x} & \frac{\partial \phi}{\partial V_y} & \frac{\partial \phi}{\partial V_z} & \frac{\partial \phi}{\partial \phi} & \frac{\partial \phi}{\partial \theta} & \frac{\partial \phi}{\partial \psi} \\ \frac{\partial \theta}{\partial X} & \frac{\partial \theta}{\partial Y} & \frac{\partial \theta}{\partial Z} & \frac{\partial \theta}{\partial V_x} & \frac{\partial \theta}{\partial V_y} & \frac{\partial \theta}{\partial V_z} & \frac{\partial \theta}{\partial \phi} & \frac{\partial \theta}{\partial \theta} & \frac{\partial \theta}{\partial \psi} \\ \frac{\partial \psi}{\partial X} & \frac{\partial \psi}{\partial Y} & \frac{\partial \psi}{\partial Z} & \frac{\partial \psi}{\partial V_x} & \frac{\partial \psi}{\partial V_y} & \frac{\partial \psi}{\partial V_z} & \frac{\partial \psi}{\partial \phi} & \frac{\partial \psi}{\partial \theta} & \frac{\partial \psi}{\partial \psi} \end{bmatrix} \quad (3.17)$$

The measurement model will be considered as an identity matrix since initially the measurement is obtained from a GPS, which is directly related with the states. Once the system disconnects its GPS, the measurement model changes completely to the Geomagnetic mapping along with its Covariance R.

$$\hat{H}_{k-1}^T = \begin{bmatrix} 1 & 0 & 0 & 0 & 0 & 0 & 0 & 0 & 0 \\ 0 & 1 & 0 & 0 & 0 & 0 & 0 & 0 & 0 \\ 0 & 0 & 1 & 0 & 0 & 0 & 0 & 0 & 0 \end{bmatrix} \quad (3.18)$$

Once the Jacobians are analytically calculated, the matrices Q and R are tuned as design parameters of the filter, so Equations can be used iteratively to estimate the states of the system. The EKF will predict the next state through the nonlinear equations and will update the the predictions with the observations at each iteration.

### 3.4. Simulation Environment

To implement and understand each of the sub-algorithms involved in the Geomagnetic Aided Navigation system, as the EKF, INS, MAD, GMA, and NEDP, a simulation environment was built using MATLAB and Simulink. This Simulation scheme is composed by a trajectory generator that provides the position references, the control module that drives the vehicle according the given reference, the quadcopter dynamics based on the equations of motion, and the GAN algorithm presented in Figure 3.1.

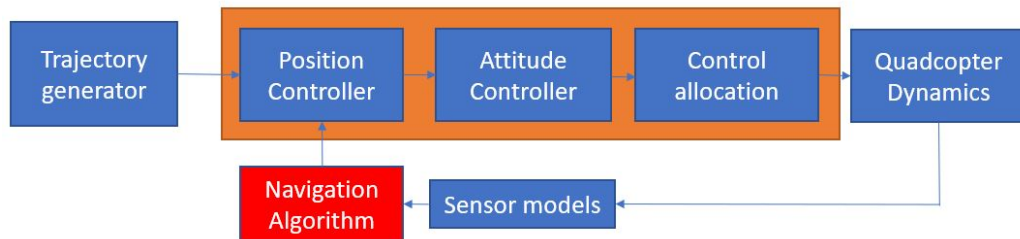


Figure 3.13 Simulation environment architecture

### 3.4.1. Quadcopter Dynamical Model

The quadcopter selected to be simulated corresponds to a 3DR x8 model as shown in Figure 3.14, available at the Advanced Dynamics and Control Laboratory at ERAU. To calculate the constants required by the Equations 2.11, a CAD model of the real system was created as shown in Figure 3.15. Additionally, A first order transfer function was used to simulate the response of the motors in the simulation environment where a voltage input will induce a proportional rotational velocity with a small settling delay (Brindha et al., 2011).



Figure 3.14 3DR Quadcopter Available Selected for Testing



Figure 3.15 3DR CAD model Representation built in Autodesk Inventor

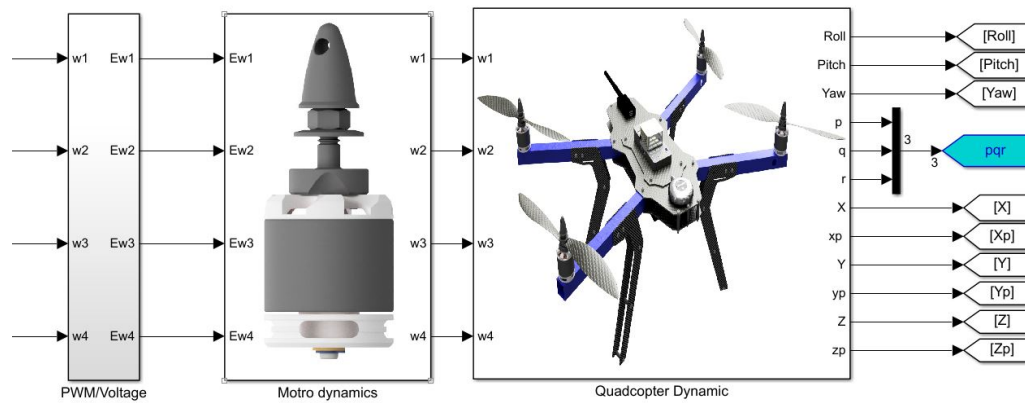


Figure 3.16 Simulink Blocks implemented for the Quadcopter dynamics

By combining the mathematical models of the quadcopter and the motor, the quadcopter Dynamical block was implemented as shown in Figure 3.16.



### 3.4.2. Quadcopter Control Model

A block capable of converting position references to the Quadcopter's input commands was built as presented in Figure 3.18, based on nonlinear control theory. This block runs a Non-linear Dynamic inversion control system in the background divided into two loops, the inner controller that handles the attitude and the outer controller that handles the position as shown in Figure 3.17. A detailed explanation of the control laws can be found in (Rivera, 2018).

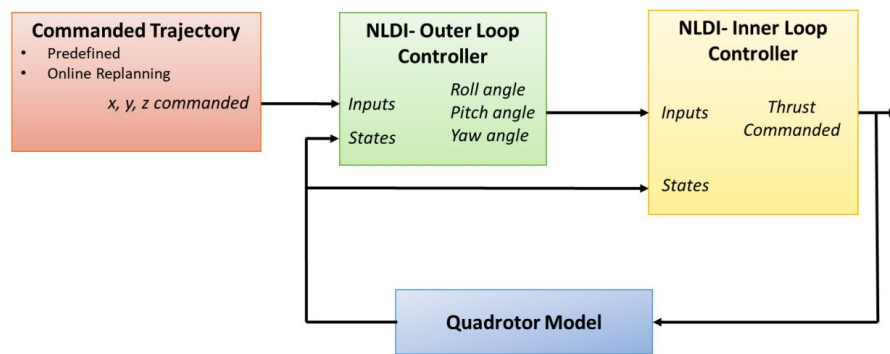


Figure 3.17 NLDI Controller Architecture (Rivera, 2018)

Since the quadcopter dynamical model receives the motor's angular velocities as inputs, and the control module outputs the required moments and forces to achieve the reference trajectory, a control allocation model is applied as shown in Figure 3.19. This will act as an adapter between these two models. The equation for this block can be determined by inverting the expressions in (2.10) (Luukkonen, 2011).

### 3.4.3. Trajectory Generation

The control block draws a set of time-dependent inputs that set the reference position, that is,  $X(t)$ ,  $Y(t)$ ,  $Z(t)$ , and  $Yaw(t)$ . In this way, the controller is implicitly informed of the speeds and accelerations required. Additionally, these trajectories must satisfy continuity and differentiability. An example of the kind of trajectories required by the Simulink model is presented in Figure 3.20, where continuous time dependent positions  $X$ ,  $Y$  and  $Z$  are defined as reference of the simulation.

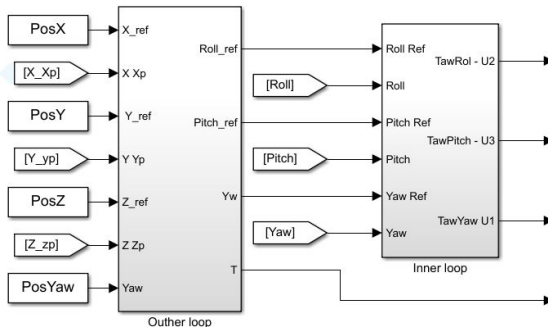


Figure 3.18 NLDI blocks implemented in the Simulation environment

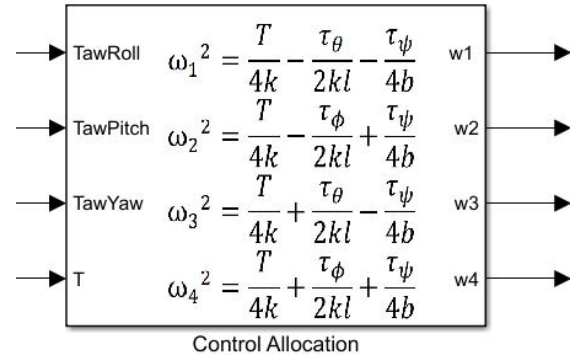


Figure 3.19 Control allocation block as interconnection block

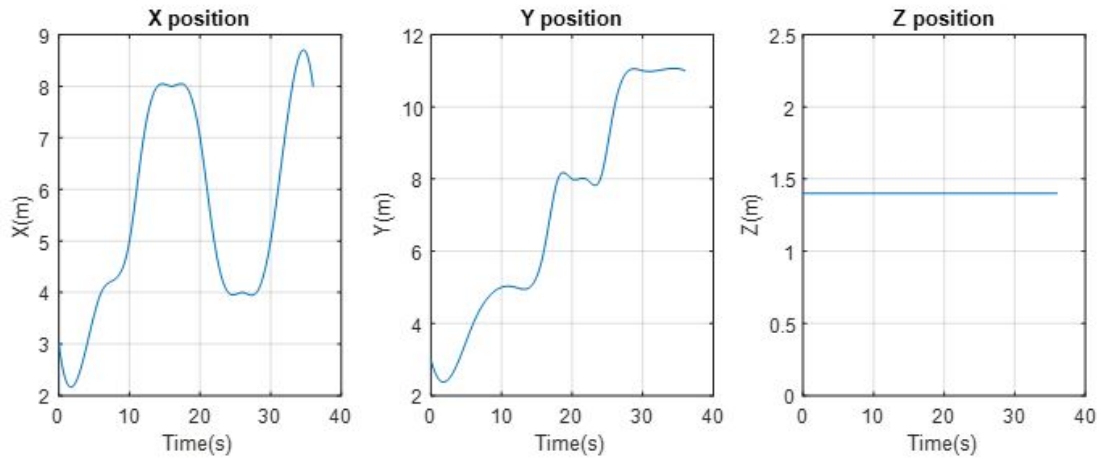


Figure 3.20 Decomposed Time-dependent Trajectory

One way to comply with this requirement is to use Matlab's spline tool to generate a time dependent curve for each of the references. It only requires a set of vectors for each reference, all of which is described by a time vector of the same size.

#### 3.4.4. GAN Implementation

The GAN algorithm is implemented as described in figure 3.1. It is composed by four subsystems, the sensor models, the main Extended Kalman filter with the INS, the Geomagnetic Matching algorithm and the Nearest Euclidean Distant Point calculation. Each of the algorithms were implemented and combined together in Simulink along the Quadcopter model to close the Simulation loop.

#### 3.4.4.1. Sensor Models

Matlab Toolboxes were used to develop models for GPS, and IMU components. For the magnetometer's specific case, Matlab uses the World magnetic model as the source, but as defined in Chapter 2, due to the selected test area size, the resolution of the World magnetic model is not applicable. Notwithstanding, the data from the measured or approximated maps in Figures 3.5 and 4.5, can be used for this purpose. The sensor model determines the magnetic value by using Equation 4.1 with current position, and adds Gaussian white noise with mean zero and covariance as shown in Figure 3.21.

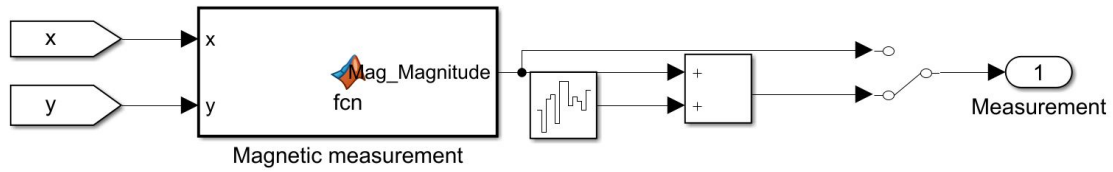


Figure 3.21 Magnetometer Sensor model

A typical GPS provides position and velocity measurements at 5Hz rate. To model this system, the real position is used as a baseline, and a rate transition is integrated to deliver the data at a similar rate. Additionally, Gaussian noise with mean zero and covariance 0.01 is added to the output as show in figure 3.22.

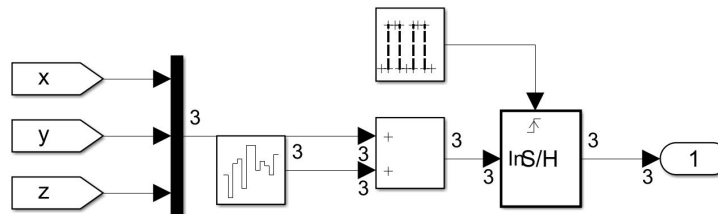


Figure 3.22 GPS Sensor model

The three-axis inertial measurement block included in the navigation toolbox models the IMU sensors as Second-order dynamics. This block include noise addition to the signal and returns the values in body inertial frames. The noise power used in this block is 0.001 for accelerometer and 0.0001 for the gyroscope.

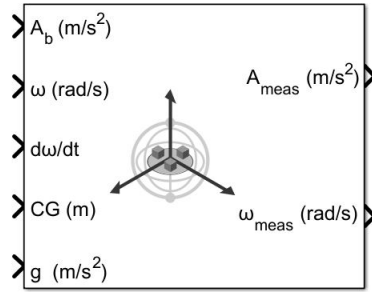


Figure 3.23 Three-axis inertial measurement unit in Matlab's Navigation Toolbox

#### 3.4.4.2. INS - Extended Kalman Filter

The implementation of the EKF filter in Simulink follows Equations (2.1) to (2.25), where the transition and measurement matrices are matrices (3.17) and (3.20), respectively. This algorithm was coded and implemented in block as shown in Figure 3.24. The process noise covariance matrix  $Q$  is picked as convenience since it is one of the filter design inputs, while the  $R$  matrix is a diagonal matrix with covariance from the GPS sensor model. These matrices are defined in the block as follows:

$$Q = \begin{bmatrix} 10^{-5} & 0 & 0 & 0 & 0 & 0 & 0 & 0 & 0 \\ 0 & 10^{-5} & 0 & 0 & 0 & 0 & 0 & 0 & 0 \\ 0 & 0 & 10^{-5} & 0 & 0 & 0 & 0 & 0 & 0 \\ 0 & 0 & 0 & 10^{-2} & 0 & 0 & 0 & 0 & 0 \\ 0 & 0 & 0 & 0 & 10^{-2} & 0 & 0 & 0 & 0 \\ 0 & 0 & 0 & 0 & 0 & 10^{-2} & 0 & 0 & 0 \\ 0 & 0 & 0 & 0 & 0 & 0 & 10^{-8} & 0 & 0 \\ 0 & 0 & 0 & 0 & 0 & 0 & 0 & 10^{-8} & 0 \\ 0 & 0 & 0 & 0 & 0 & 0 & 0 & 0 & 10^{-8} \end{bmatrix} \quad (3.19)$$

$$R = \begin{bmatrix} 0.01 & 0 & 0 \\ 0 & 0.01 & 0 \\ 0 & 0 & 0.01 \end{bmatrix} \quad (3.20)$$

The Jacobian was precalculated with Matlab and scripted inside the Kalman filter block. The states update uses the discrete nonlinear equations, and the sample time defined is 0.01 for simulation purposes.

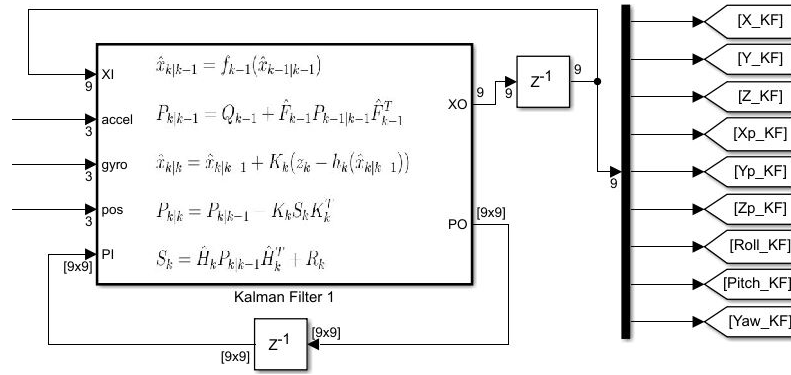


Figure 3.24 Extended Kalman filter block

#### 3.4.4.3. Map Matching and Contour Approximation

The Geomagnetic Aided Navigation block is solved in two steps, the Map Matching and Closest contour point (NPED). Both algorithms are integrated together in the same block and were implemented in sequential form, similar to how it should be implemented in a micro-controller for implementation. The GAN block is connected to the INS and sensor models as presented in Figure 3.25. Additionally, a block to switch between the GPS signal and the GAN estimation is included at the Inertial Navigation System's position input. This allows to exchange the position measure and test the performance of the GAN method when the GPS is disconnected.

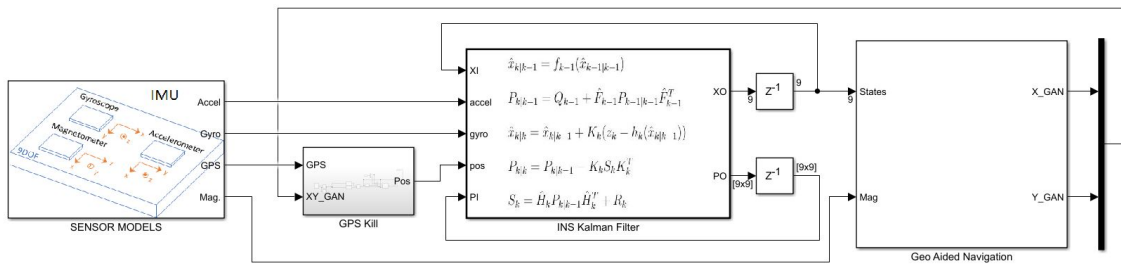


Figure 3.25 GAN Simulink blocks architecture

### 3.4.5. Graphical Interface

A Matlab script was developed to graphically interpret the data produced by the quadcopter trajectory tracking and the GAN estimation results as shown in Figure 3.26. The quadcopter is plotted in a 3D environment, and the contour map is shown along with the Uncertainty area, the measurement contour line in the area, the real position and the estimated one. This allows to detect conditions when it can deviate.

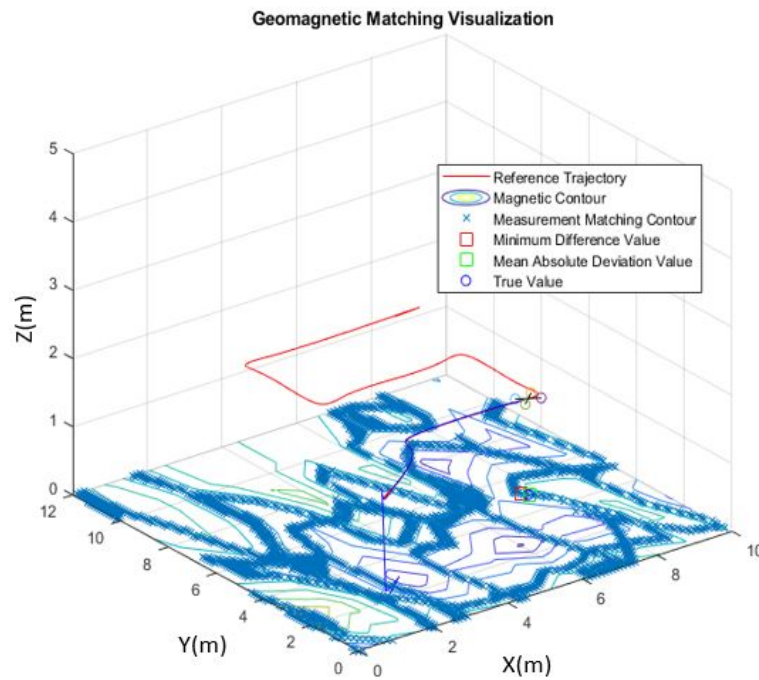


Figure 3.26 Graphic interface Visualization

The minimum inputs required to use this visualization method are the position and orientation history of the mission. On top of it, additional available data can be added as magnetic maps, uncertainty areas, GAN estimation, INS estimation, between others.

### 3.5. Experimental Setup

A 3DR Quadcopter was instrumented with the goal of collecting data from the field and process it with the GAN algorithm as an alternative of the simulated generated data. This section is divided into the hardware setup, software description and the experiment definition.

### 3.5.1. Hardware

The PX4 Autopilot is an opensource board developed by contributors from the industry and Academia to power all kind of aerial or ground vehicles. The firmware includes features as estimators, autonomous control, flight modes, safety features and has extended support for airframes, telemetry systems, RC controllers and vehicles.



Figure 3.27 PX4 V4 Autopilot.



Figure 3.28 PX4 Pixhack V5 Autopilot

The Frame is an 3DR RTF X8 structure composed of aluminium bars and carbon fiber body, converting this quadcopter a lightweight model compared to its size. It is powered by a 4S 10000mAh battery and four T-Motor MT2216-9 1100KV Brushless motors combined with 10x3.3 Carbon fiber propellers. This setup provides a strong weight/lift ratio and extended flight time.



Figure 3.29 T-Motor MT 2216-9 1100kV

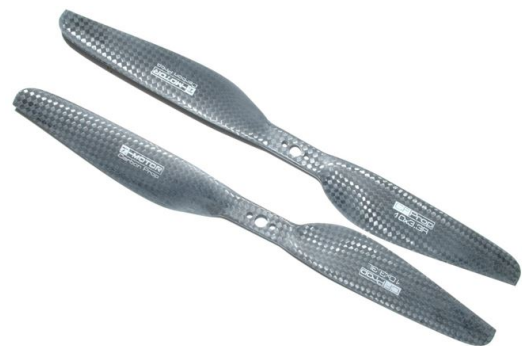


Figure 3.30 T-Motor 10x3.3 Propellers



The flight controller is handled by a PX4 V5 programmed with Mission Planner, and the firmware version used was the ARDUCOPTER V3.611. The microstrain sensor was mounted at the center of the body with its GPS. The data from these devices was obtained through another PX4 board programmed with the Matlab Embedded support package for PX4. The Figure 3.31 displays the setup with the electronics on-board.

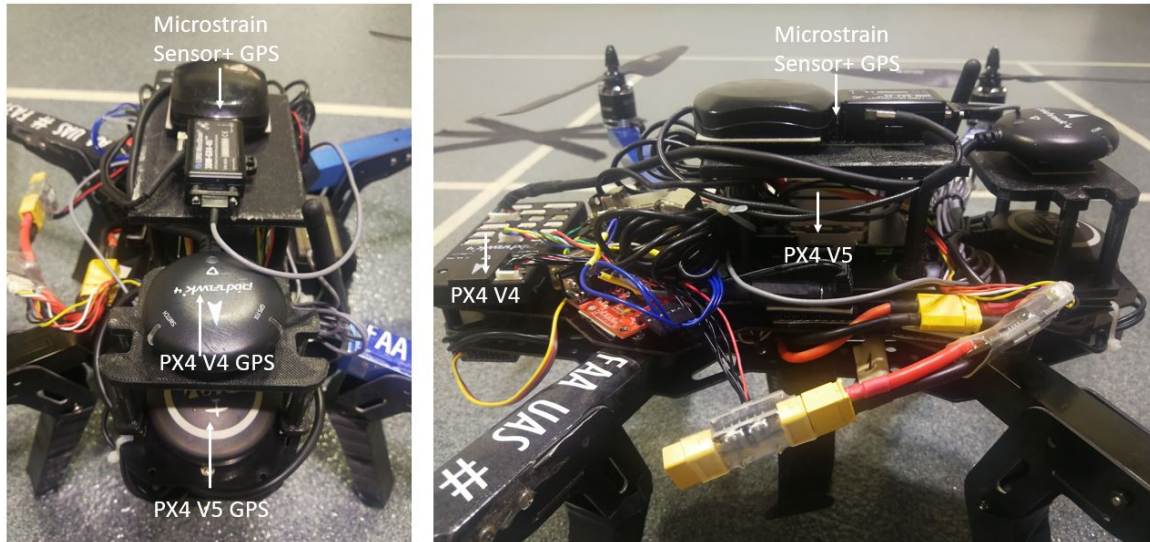


Figure 3.31 3DR Quadcopter Setup

A PX4 V4 will record the GPS data from secondary devices as redundancy along with the microstrain sensor. The specification of the IMU sensor of the microstrain and PX4 V4 are presented in the Table 3.2 and Table 3.3. The Microstrain sensor is considered the primary source of information due to its increased accuracy against the PX4 V4.

Table 3.2

#### Microstrain Accelerometer/Gyroscope Specifications

(“Microstrain 3DM-gx4-45 Datasheet”, 2016)

Parameter	Accelerometer	Gyroscope
Noise Density	$100\mu g/\sqrt{Hz}$	$0.005^\circ \text{ sec}/\sqrt{Hz}$
Measurement range	+/- 5g	+/-300°/sec
Initial Bias error	+/-0.002g	+/-0.05°/sec
Alignment Error	0.05°	0.05°



Table 3.3

## PX4 V4 Accelerometer/Gyroscope Specifications

(“High Performance 6-Axis MEMS MotionTracking”, 2018)

Parameter	Accelerometer	Gyroscope
Noise Density	$210\mu g/\sqrt{Hz}$	$0.01^\circ \text{ sec}/\sqrt{Hz}$
Measurement range	$\pm 2g$	$\pm 250^\circ/\text{sec}$
Initial Bias error	$\pm 0.080g$	$\pm 5^\circ/\text{sec}$

### 3.5.2. Software

The PX4 V5 Flight control’s Firmware was programmed using the mission planner software shown in Figure 3.32, on the PixHack V5 for a quadcopter 4 motors Airframe. The software’s wizard helps through the set up of the controller, the sensor calibration, flight modes, and RC. Additionally, data can be streamed back to a computer by connecting the vehicle to the mission planner with telemetry antennas.



Figure 3.32 Mission planner interface (Ardupilot, 2020)

Matlab has included the PX4 platform in its pool of toolboxes by developing an interconnection between Simulink and the PX4 Autopilot. Thanks to this, it is possible to access the PX4 firmware features from Matlab/Simulink, implement custom controllers or algorithms and generate the corresponding C-code using Matlab’s Embedded coder support package into the Hardware.

The ADCL had developed a Simulink block in Figure 3.33 capable of requesting and reading the sensor data from the Microstrain through serial communication. By using these blocks and the Embedded coder Support package for PX4 Autopilots, it was possible to collect data from flight testing along with the IMU from the board.

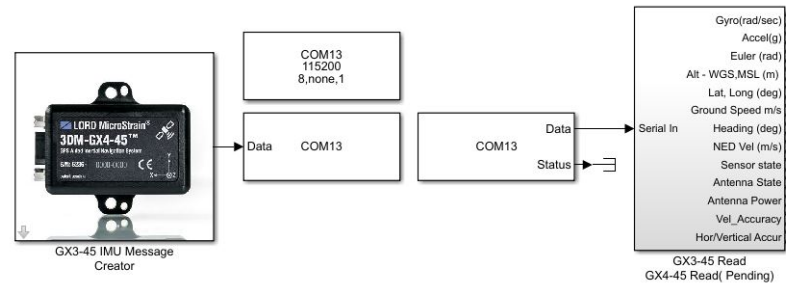


Figure 3.33 Simulink block for Microstrain data reading. ADCL Implementation

### 3.5.3. Data Collection

Different sets of flights were performed to collect sensor data from the field and assess the effects of the vehicle and its dynamics in the measurements. Additionally, GPS data was recorded as the position reference value during all the flights. The data recorded is saved in the PX4 SD card and requires a post processing in Matlab to be used as the reference data for the GAN architecture implemented.



Figure 3.34 Collection data Flight performed at Embry-Riddle's Softball Field

First, the PX4 local position estimation is given in the NED reference frame with the origin of where the vehicle is powered. This frame was found to be  $+29.5^\circ$  tilted from the frame selected for the test area. By using the rotation matrix in Equation (2.4), this angle is corrected, so the positions given by the PX4 match the grid frame. Subsequently, since the gyroscope and accelerometer data are measured in the body frame, no processing is required. Last, the magnetometers measure the field's components in the body frame axis, but since the magnitude should remain equal seen from any reference frame, no transformations are required. Therefore, the magnitude is calculated from the vector components.

## 4. Results and Analysis

This Chapter is focused on presenting and analyzing the results obtained from the implementation of the algorithms by running different sets of data from the simulation environment and real external data. Moreover, it aims to answer questions regarding the implementation of the algorithms by identifying consequent problems associated with the real world implementation.

### 4.1. Geomagnetic Fingerprint and Contour Lines

One of the magnetic field's main assumptions is that it is constant over time. This statement holds when referring to periods close to a couple of years without considering day-night cycle inferences. To evaluate this statement, an experiment was conducted at the indoor facility at ADCL of ERAU, consisting of measuring the room's magnetic field at 1m height, at 3 different days at different times.

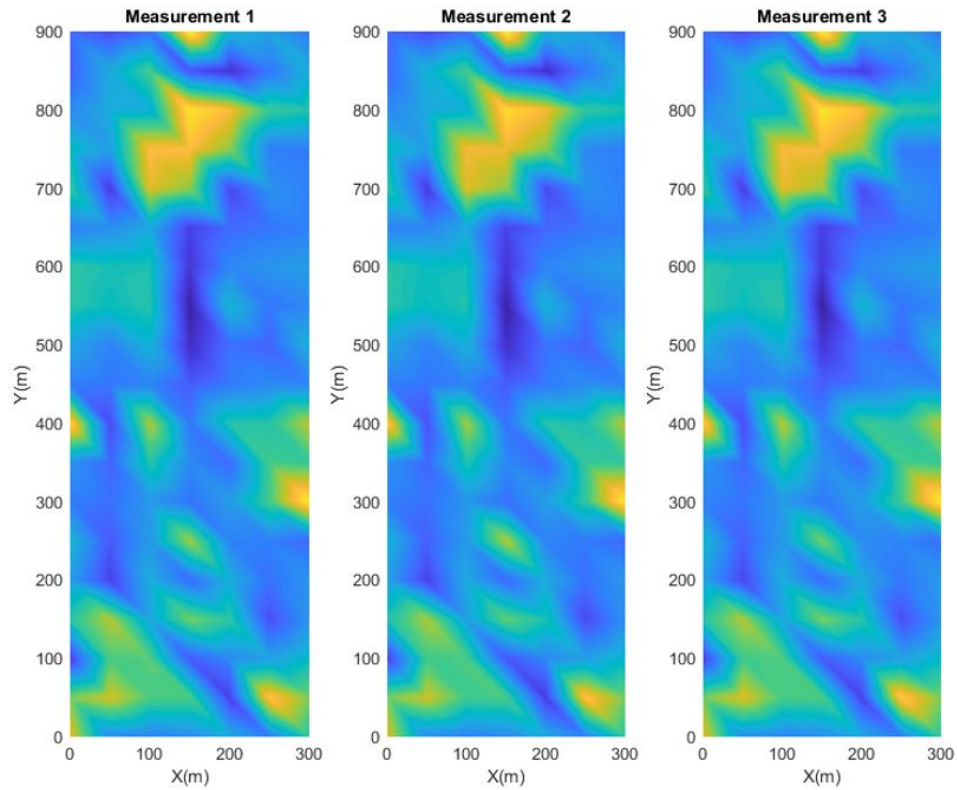


*Figure 4.1* Indoor Facility - Magnetic field measurements.

Three magnetic fingerprints were obtained each from different days as presented in Figure 4.1, with no major changes. Still, it was expected then to observe small variances when it concerns to outdoor tests since no structural disturbances are present in the field. Subsequently, a second test was conducted using the data collected from the indoor facility, which intends to confirm that a measurement can be linked to a contour line, and the position where the measurement was taken should be inside in the respective contour.

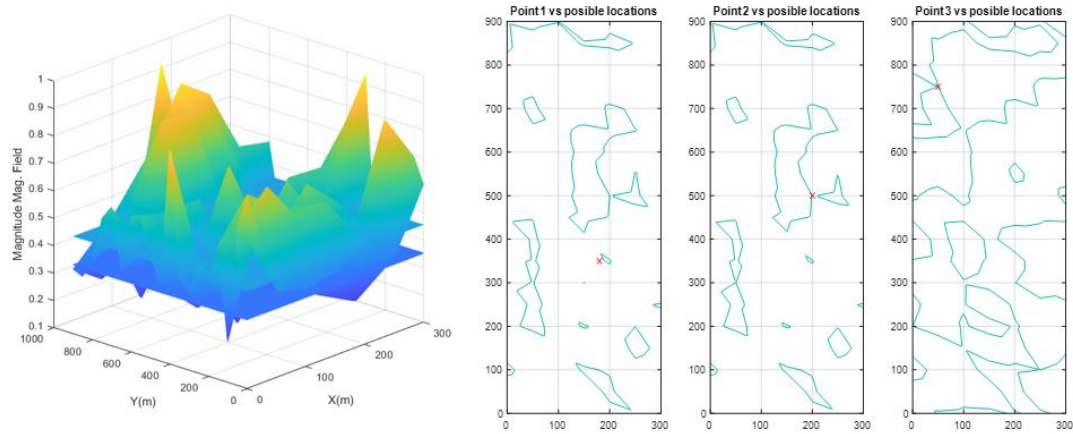


*Figure 4.2* Indoor Facility - Point locations experiment Results.

As presented in Figure 4.2, three different points at the facility were randomly selected, and their magnetic magnitude was measured. Subsequently, the contour line related to each measurement was obtained for each case by crossing a plane (The magnitude measured) with the surface and finding the intersections. The real position was marked with a red X on each line. For each case it was observed that the real point was close to its respective line. It is important to mention that a sensor has noise normally described as Gaussian with an assigned covariance. By knowing the covariance of the sensor, it is possible to analyze what implications the noise has with the contour line probability, as shown for example in the Figure 4.3. When the Equation (2.15) is evaluated given a magnetic measure with defined noise covariance with zero mean, its probability is not defined anymore by a line but by an area.

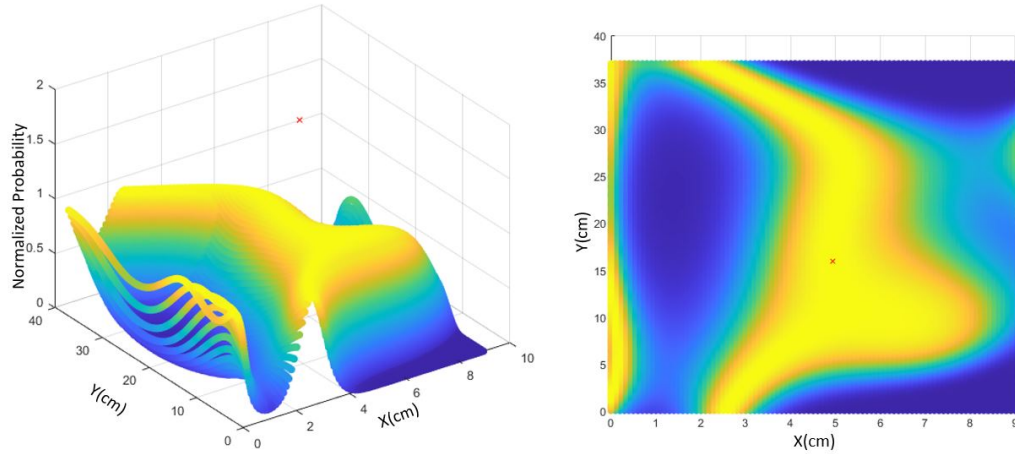


*Figure 4.3* Probability density function observed from the Geomagnetic Map

The experiments performed in the indoor facility aimed to verify concepts that supports the usability of magnetic fields for position localization, but since this study focuses on outdoors applications, the algorithms are tested with the geomagnetic data obtained at the outdoor facility field.

Once defined the magnetic map from the measurements as presented in the Figure 3.5, an interpolation of the data is performed so the initial 10x38 grid is then refined into a new grid of size 91 by 371 as presented in Figure 4.4. By the other hand, the map is approximated into a polynomial surface using the Matlab fit tool, obtaining the map presented in Figure 4.5. By evaluating different fittings as presented in Table 4.1, a 5th order approximation is selected since its chi-squared value is the closest to one.

Table 4.1

Reduced Chi-Squared Goodness-of-fit metric

Fit	# Parameters	Red. Chi-Squared
<b>poly23</b>	9	3.58
<b>poly33</b>	10	3.44
<b>poly44</b>	15	4.74
<b>poly55</b>	21	3.05



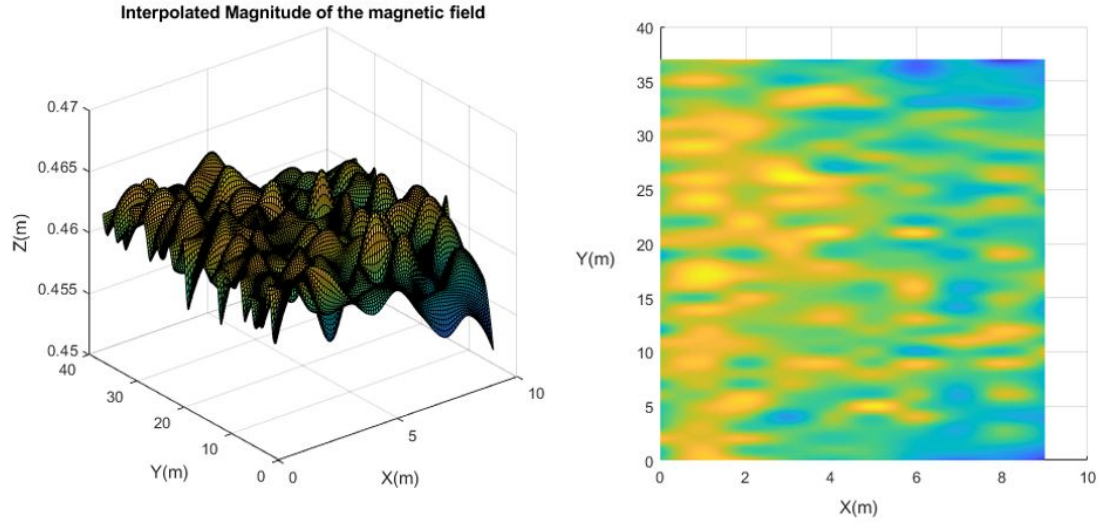


Figure 4.4 Interpolated Field's Magnitude map from data of Figure 3.5

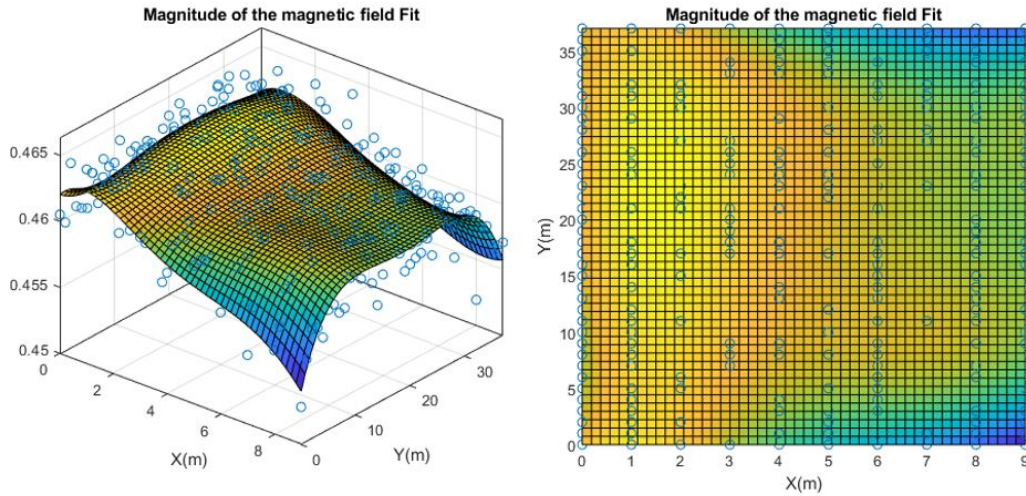


Figure 4.5 Approximated Field's Magnitude map from data of Figure 3.5

The resulting polynomial approximation has 21 identified parameters, described in the Equation 4.1. According to its Chi-squared value greater than one, there may exist a better approximation or improvements can be done. This may reflect the consideration that the noise in the measurements is not completely captured by the approximation.

$$\begin{aligned}
H(x, y) = & 0.462 + 2.47 \cdot 10^{-3}x - 3.6 \cdot 10^{-4}y - 1.84 \cdot 10^{-3}x^2 + 1.8 \cdot 10^{-4}xy + 4.575 \cdot 10^{-5}y^2 \\
& + 3.9 \cdot 10^{-4}x^3 + 1.514 \cdot 10^{-5}x^2y - 1.96 \cdot 10^{-5}xy^2 - 1.97 \cdot 10^{-6}y^3 - 3.61 \cdot 10^{-5}x^4 \\
& - 3.479 \cdot 10^{-6}x^3y - 4.297 \cdot 10^{-8}x^2y^2 + 7.53 \cdot 10^{-7}xy^3 + 3.46 \cdot 10^{-8}y^4 + 1.125 \cdot 10^{-6}x^5 \\
& + 2.56 \cdot 10^{-7}x^4y - 1.13 \cdot 10^{-8}x^3y^2 + 3.16 \cdot 10^{-9}x^2y^3 - 1.01 \cdot 10^{-8}xy^4 - 2.05 \cdot 10^{-10}y^5
\end{aligned}
\tag{4.1}$$

From the Magnetic map recreated from the Softball Field, two contrasting contour maps are defined in Figure 4.6. The first at the left corresponds to the interpolated data from Figure 4.4, and mostly it is delineated by the noise of the sensor and possibly human errors in the measurement procedure. The second contour from Figure 4.6 draws the the map of the Figure 4.5. This is an approximation of the measured map that aims to mitigate the noise from the interpolated one. As starting point, the approximated map will be used to develop the simulation cases.

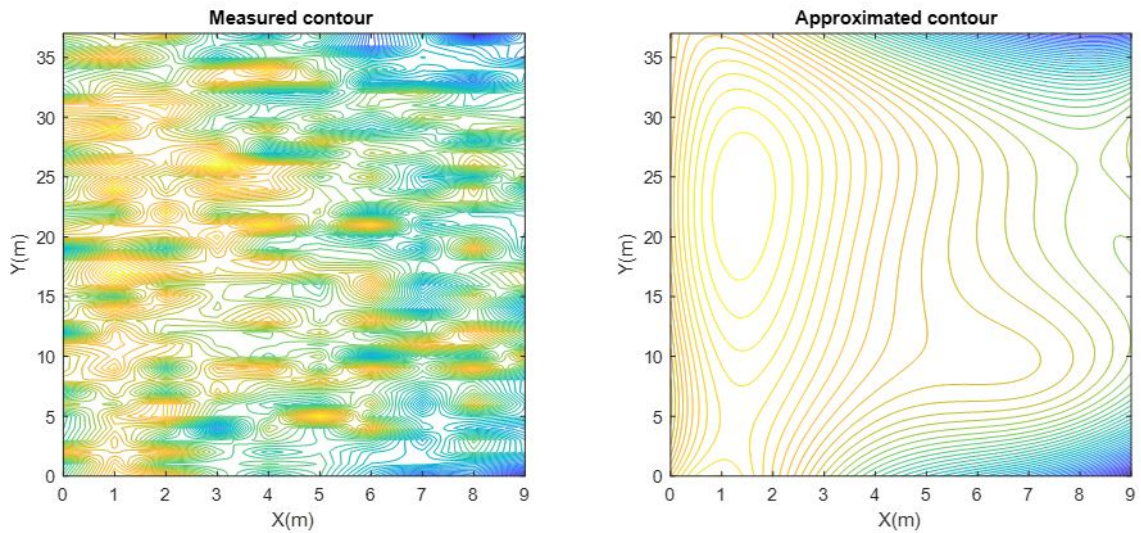


Figure 4.6 Measured and approximated contours

## 4.2. Trajectory Generation

Using the Simulation environment, it is possible to create different trajectories over the field, along with the data previously collected. This is very useful to understand the algorithms from a graphical perspective.



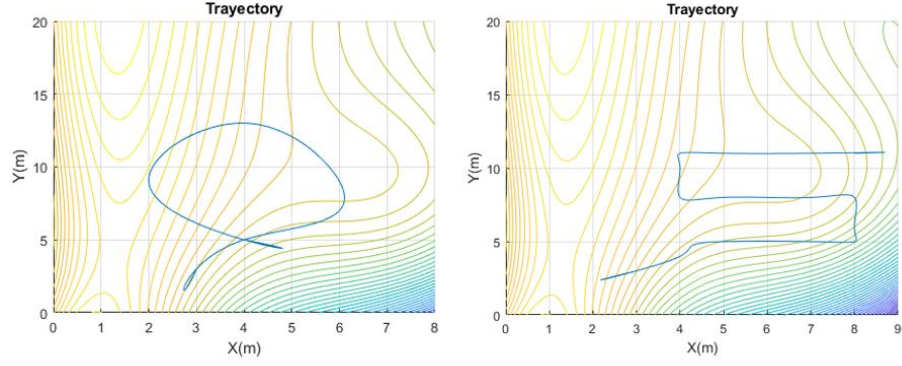


Figure 4.7 Trajectories proposed as study cases. a) O pattern, b) S pattern

The cases to be considered are a rounded pattern as displayed in Figure 4.7.a, and S pattern 4.7.b. These cases are designated as trajectory O and S, respectively. Each case generates an independent position reference set for  $X$ ,  $Y$  and  $Z$  as presented in Figure 4.8 for the O pattern, and Figure 4.9 for the S pattern. These references are used in the Simulation environment to generate sensor data for the GAN algorithm.

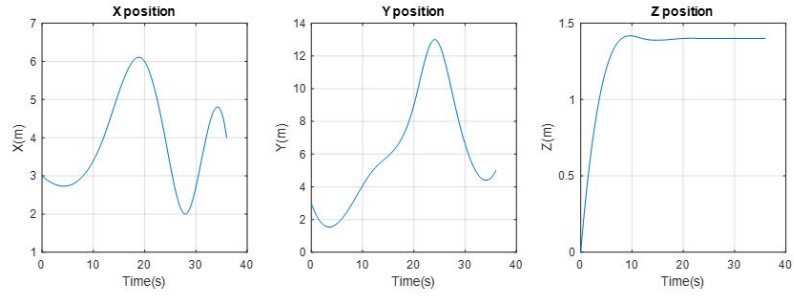


Figure 4.8 Position References for trajectory O

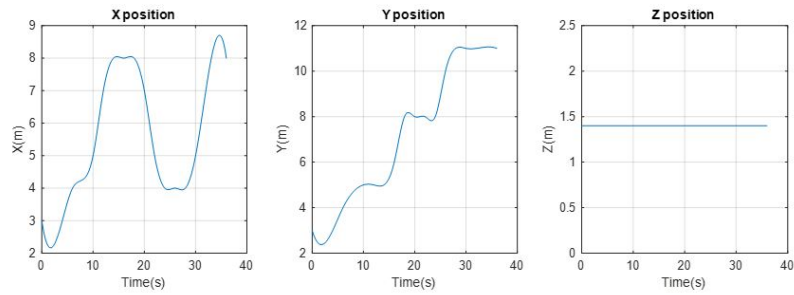


Figure 4.9 Position References for trajectory S

### 4.3. Navigation Algorithms

This section aims to present the overall improvement of the EKF over the INS, and the effect on the estimations when GPS and Magnetic data are used together, and when magnetic data is used to compensate for GPS drops. To evaluate the performance of all the navigation algorithms in different setups up to the final GAN architecture, four different cases based on GPS availability are proposed, where error metrics are evaluated. These cases are full GPS access (Position and Velocity), partial GPS access (Position), partial GPS drop (No position access) and full GPS drop (No access to position and velocities).

#### 4.3.1. Inertial Navigation System

The inertial Navigation system is implemented using Equations (3.7) to (3.15), where the state equations are integrated at each sample times, and sensor data is used to completed the missing information in the equations. Using the trajectory references from Figure 4.9, the positions and velocities from the INS calculations are presented in the Figure 4.10. The INS was tested using information only from gyroscope and accelerometer sensors.

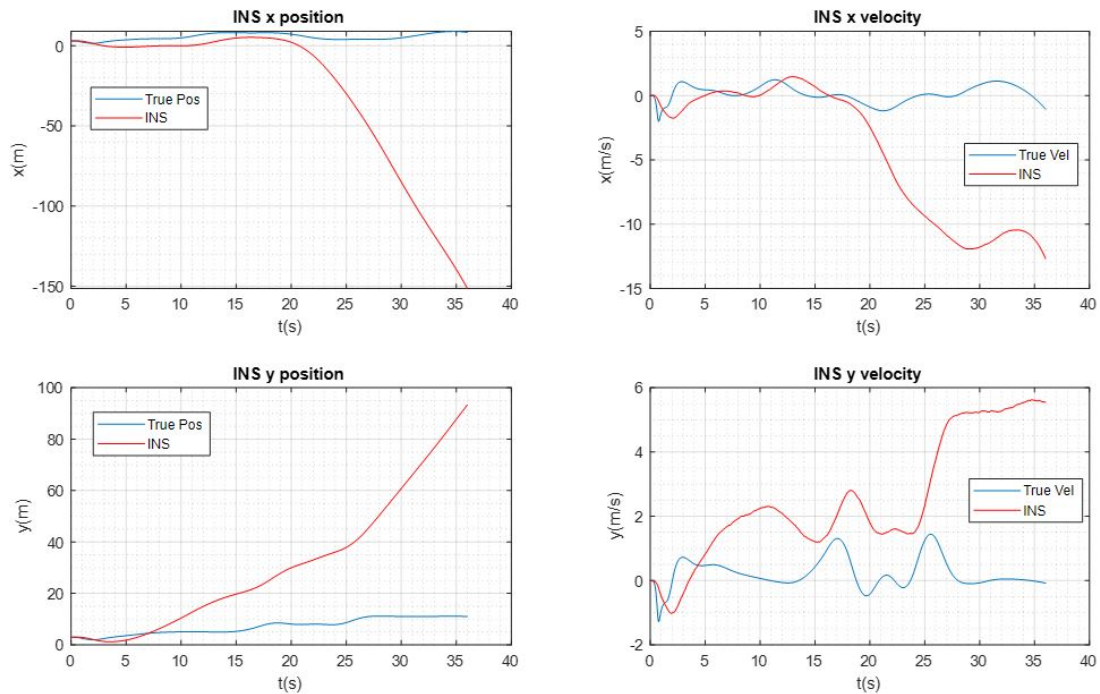


Figure 4.10 INS results for positions and velocities with gyro and accelerometer data

An intensive drift is found using only INS when no GPS information is available to correct the deviation from the error integration. Additionally, the INS as defined does not use information from GPS since in the integration process, only data from gyroscope and accelerometer is used. Therefore, drifts are observed due to the error integration. This is the reason why an Extended Kalman Filter is considered as an improvement of the INS alone.

#### 4.3.2. Inertial Navigation System - EKF

Simulations running the INS-EKF block presented in Figure 3.24 were performed for each of the cases. In this implementation, GPS was used as measurement of the position of the device. The objective of this section is to show the improvement of the position estimation by smoothing the signal coming from GPS, or later GAN system, and even when incomplete information from GPS is available. Additionally, the Table 4.2 shows a quantitative result of the INS-EKF with GAN at different GPS conditions.

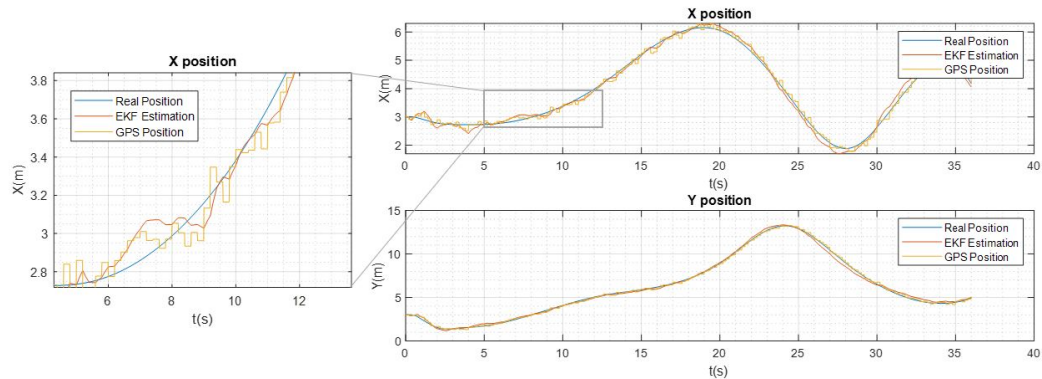


Figure 4.11 Trajectory O - EKF Position Estimation

From Figures 4.11 and 4.13, the estimation tracks the real positions closely since the EKF is tuned to trust in its measurement model, which is the GPS. When the measurement is changed to the geomagnetic position estimation, a degradation appears making it necessary to rely more on the estimation of the EKF rather than the measurement model. This means that the matrix  $R$  in the EKF should be changed when GPS is replaced for the Geomagnetic estimator, in order to reduce the confidence of the measurements and increase the confidence of the state transition model defined by Equations (3.7) to (3.15).

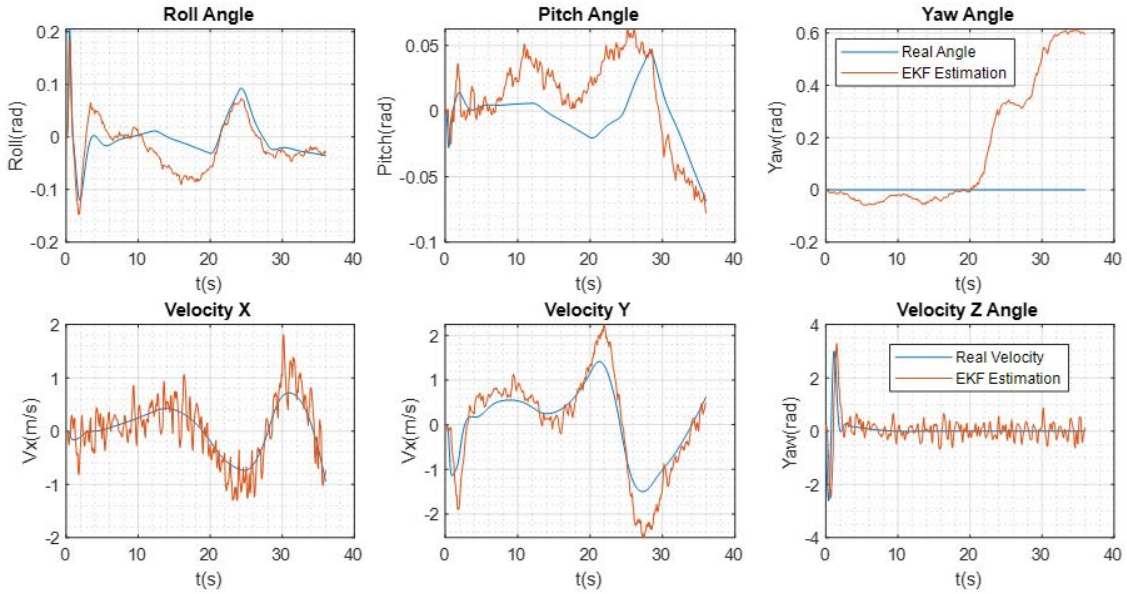


Figure 4.12 Trajectory O - States estimated by the EKF

Along with the positions, the velocities and the orientation are also estimated by the Extended Kalman filter as presented in Figures 4.12 and 4.14. The velocity is not assumed to be received by the GPS, implying that its estimation depends on the sensors' data and its correction from the position received by the GPS. The orientation angles are calculated from the sensors and the integration of the state model over time. Although errors are visible in the angle estimations, this can be refined by tuning the matrix  $Q$  of the EKF.

Some of the reasons to explain the discrepancies between the estimated values with the real ones presented in each state estimation in Figures 4.12 and 4.14 are the EKF linearization approach, its Gaussian distribution assumption, errors in the state model, and noise inclusion in sensors and processes. Additionally, it is desired to observe the influence of the addition of the geomagnetic referencing modeling in the position estimation at different cases, as for example full GPS access, only velocity information and GPS cut or drop. The performance of the EKF alone and its integration with the GAN, at the mentioned scenarios, is evaluated in the Table 4.2.

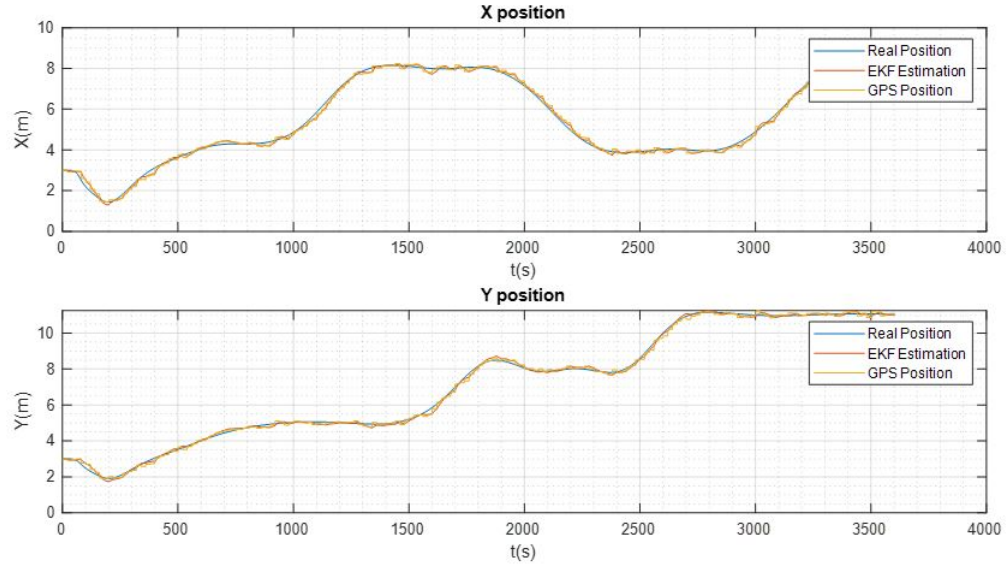


Figure 4.13 Trajectory S - EKF Position Estimation with GPS measurements

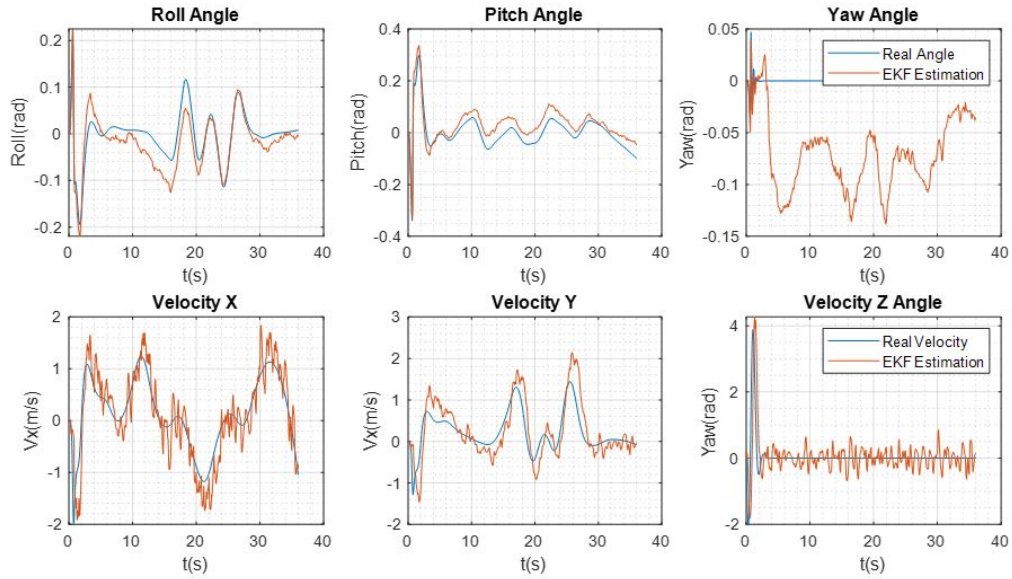


Figure 4.14 Trajectory S - States estimated by the EKF with GPS measurements

#### 4.3.3. GAN implementation

This section will show the results obtained from the schematic presented in figure 3.25, by integrating the geomagnetic matching algorithm with the Nearest Euclidean Distant Point point conforming the Geomagnetic position estimator to feedback into the EKF as presented in Figure 3.1.



#### 4.3.3.1. GMA with GPS

With the EKF defined, the geomagnetic matching algorithm and nearest contour point method are implemented as complementary modules. Along with the results obtained from the GAN algorithm, the INS and EKF cases are being presented simultaneously to reflect graphically the behavior of the algorithms. Once the algorithm is initialized, it is required to build confidence in its matching history. The matching method depends strongly in a good position measurement and its purpose is to correct the INS drift. It is possible first to evaluate the matching algorithm without using its information back in the EKF. If one desires use it, this information goes to the EKF as the previous state rather than the measurements while GPS is available.

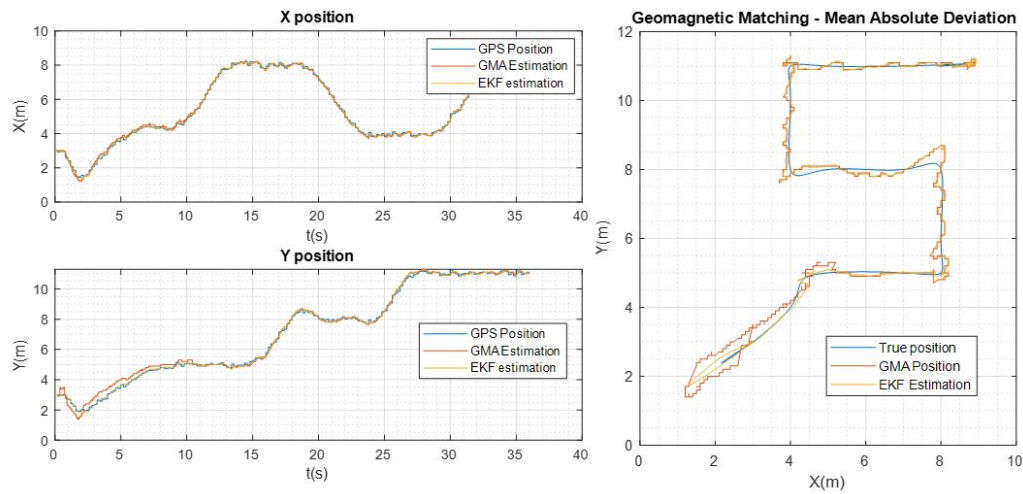


Figure 4.15 Trajectory S - Geomagnetic Matching Position estimation

From the results of both S and O trajectories shown in figures 4.15 and 4.16, the MAD algorithm converged to the INS estimation point, which is the center of the uncertainty area. This can be observed at 11s in Figure 4.15 and 13s in Figure 4.16 where the estimation has a jump in the position as described in Figure 3.10. This argues that the MAD algorithm trusts in the INS estimation, led by the GPS measurements. If one desires to feedback the matching algorithm's output as measurement, the EKF estimation will drift or converge to an incorrect point.

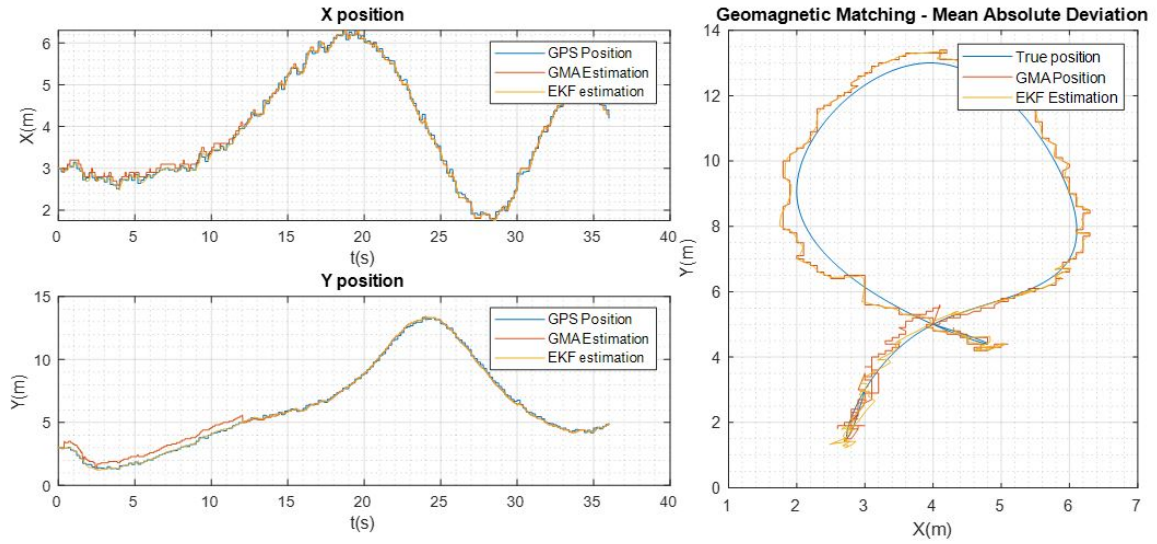


Figure 4.16 Trajectory O - Geomagnetic Matching Position estimation

#### 4.3.3.2. GAN with GPS

The NEDP block looks into the uncertainty area and approximates the point selected from the MAD algorithm in the Geomagnetic matching, to the closest position point of the contour lines that matches the measurement at that instant. This can be observed in Figure 4.17 where the blue box is the uncertainty area while the points marked by a blue X corresponds to positions with the same magnetic magnitude as the measurements inside the area. Here, Equation (3.6) is applied to obtain the closest one to the point. In Figure 4.17. The simulation environment provides visual information of all the elements that structures the GAN architecture as presented in Figures 4.19 and 4.18. When calculating the positions with the closest magnetic value as the measurement, a tolerance in the comparison can be defined. Depending on the field's features, a high tolerance can be wise to use when the surface has a distinctive slope, while a low tolerance helps to prevent drifting when the surface is even.

Figures 4.20 and 4.21 present the position estimation of both trajectories when the architecture proposed in figure 3.1 is implemented. For this cases, GPS is still used as source for the measurement model of the EKF. A slight improvement was observed when the NEDP is implemented since it deals with the initial uncertainty of the MAD algorithm.

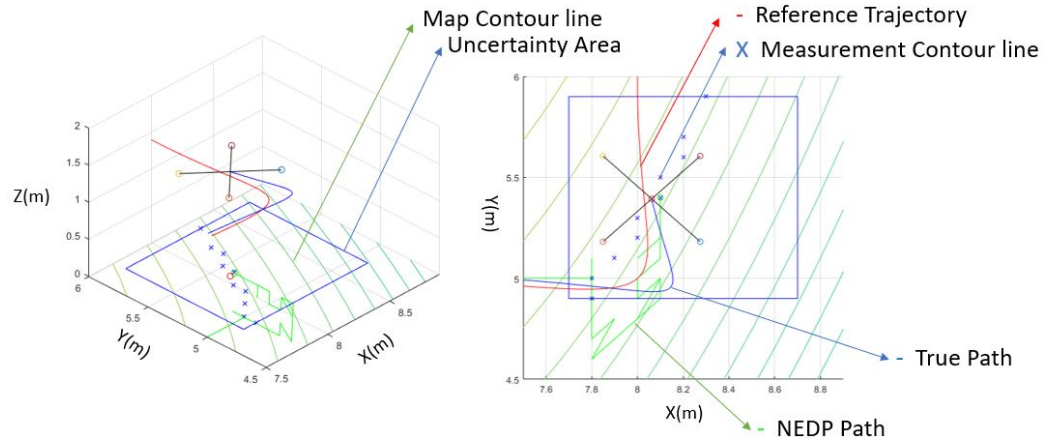


Figure 4.17 Closest Contour Point representation

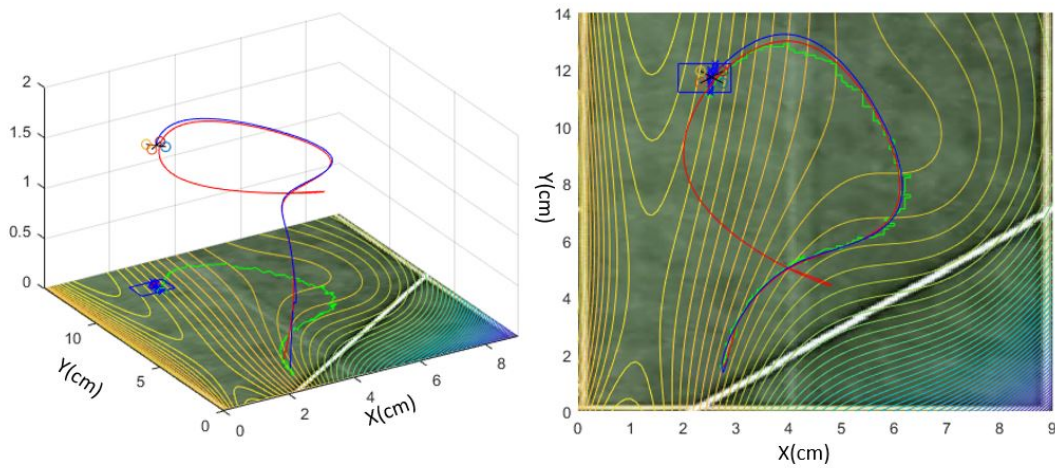


Figure 4.18 Trajectory O - 3D Visualization of GAN Path estimation

The MAD algorithm still converges to the center of the uncertainty defined by the EKF estimation. Additionally, a non-continuous pattern in the GAN estimation is observed since it depends on the resolution of the map grid. However, the information from the GAN algorithm is handled by the EKF estimation by smoothing the signal. Again, the enhancement of the position estimation with the Geomagnetic referencing while still using GPS as measurement is also being evaluated in Table 4.2 along the INS and the EKF combined with only the GMA and the full GAN structure.



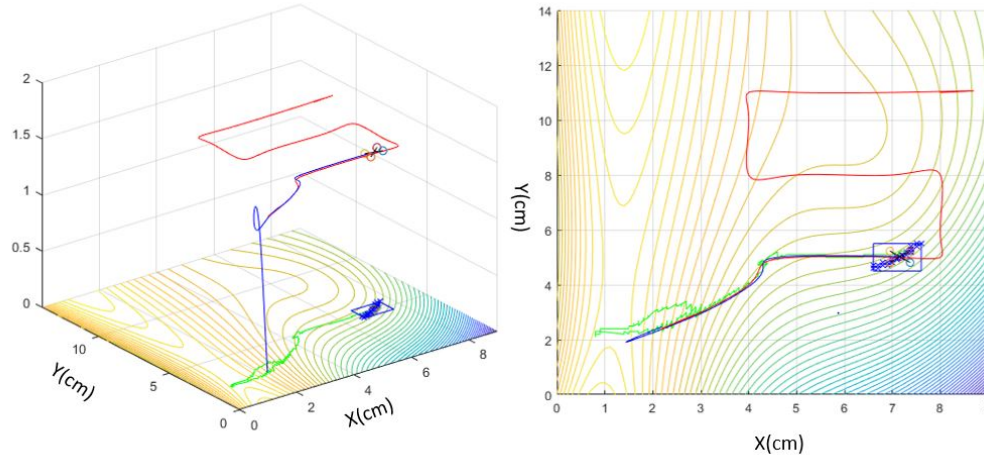


Figure 4.19 Trajectory S - 3D Visualization of GAN Path estimation

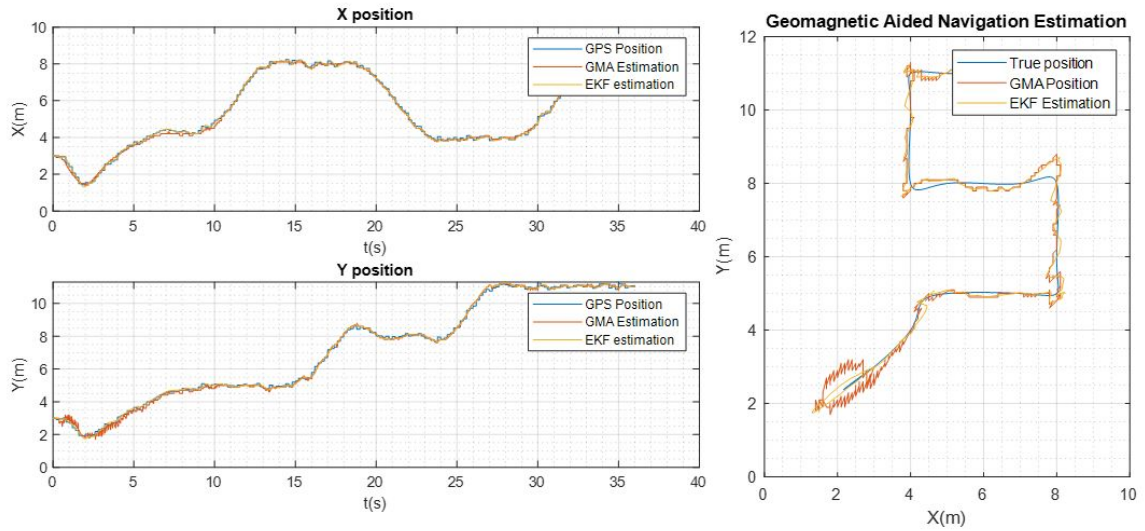


Figure 4.20 Trajectory S - Geomagnetic Aided Position Estimation

#### 4.3.3.3. GAN with No GPS

It is desired now to evaluate the degradation of the position estimation and the sturdiness of the algorithm when GPS is not available. This section presents the results obtained from different scenarios using the 3D simulation environment. First, A GPS drop was included at the interval 12s-30s, where the main EKF filter only uses now the data from the GAN algorithm as observation data instead of the GPS. The GAN algorithm is initialized from the beginning of the simulation, so it is contemplated that it has built reliance over its approximation while using the GPS.

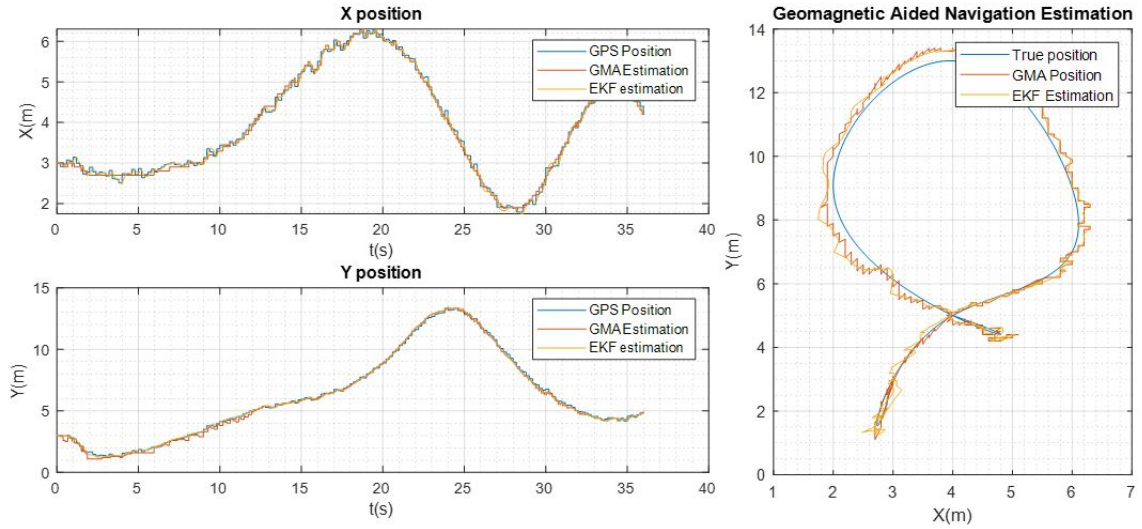


Figure 4.21 Trajectory O - Geomagnetic Aided Position Estimation

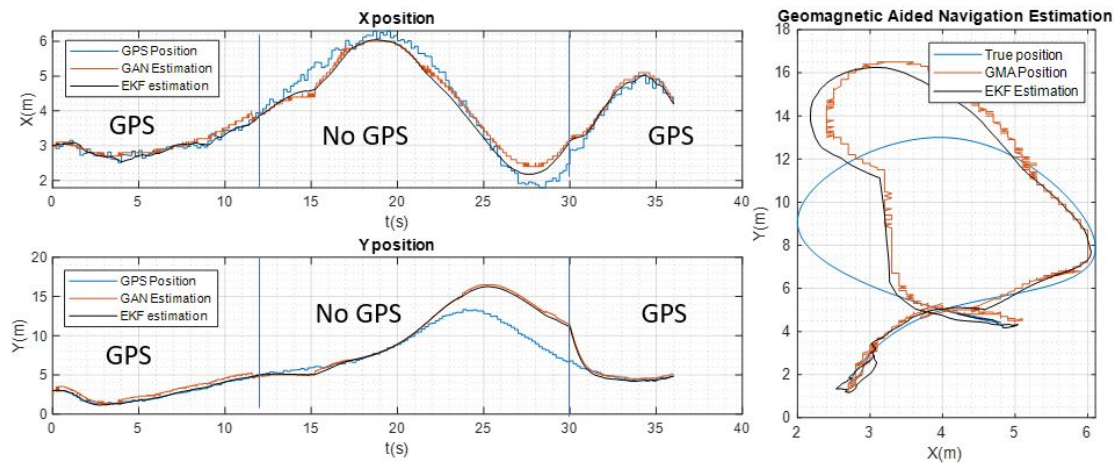


Figure 4.22 Trajectory O - GAN Position Estimation with no GPS at 11s-30s

As shown in Figures 4.23 and 4.22, when GPS drop condition is given, a degeneration of the estimation is observable when comparing the estimation against the real positions. Still, the tracking based on the magnetic contour follows the same shape as the real position. One of the key requirements observed is that this approach can be enhanced by using a good Velocity estimation. This will highly increase the accuracy of position estimation. on the other hand, there exist multiple conditions that may affect the accuracy of the algorithm that has to be identified before to plan.

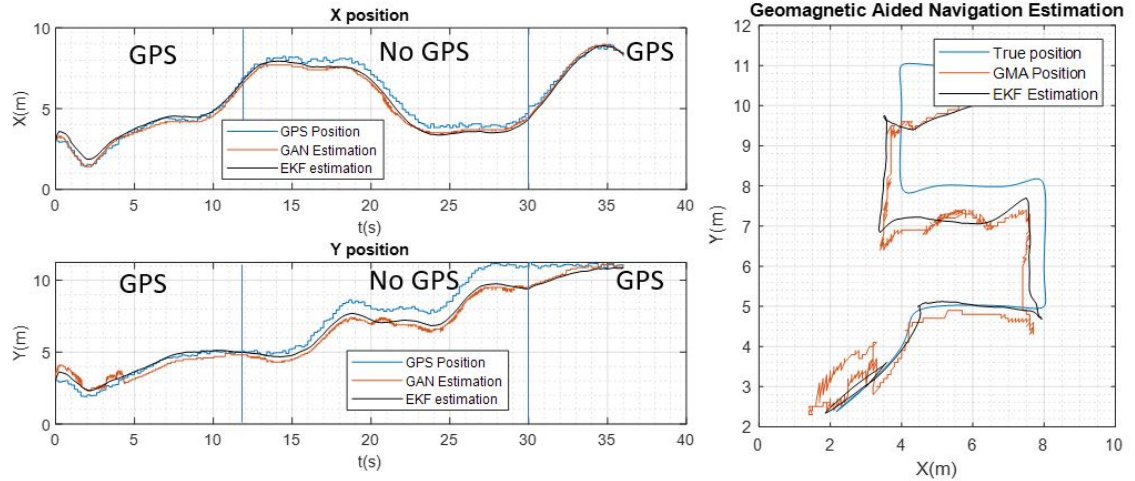


Figure 4.23 Trajectory S - GAN Position Estimation with no GPS at 11s-30s

An example of possible conditions that may affect the algorithm's performance is the selection of the path that best uses the magnetic field features as a patch that avoid flat areas that may confuse the algorithm. This is the case observed in Figure 4.22, where the Quadcopter falls in an area where the magnetic field is flat in its surroundings denoted by the uncertainty area being marked almost in its totality with X markers, meaning that all the area has the same magnetic value. Last, a comparison between geomagnetic referencing model supporting INS and EKF when a GPS drop occurs is evaluated as presented in Figure 4.24. By using this information, a metric evaluations is presented in Table 4.2, analysing the overall squared error.

#### 4.3.3.4. Consideration of Failing conditions

The GAN algorithm is susceptible to drift while not supported by a good initial guess from the INS or EKF, and requires a good estimation of the other states as the velocities. These states will define the course of observability since a wrong clue may lead to the wrong path while satisfying the magnetic matching conditions. From the case of study in Figure 4.22, the event where the estimation can be misled by multiple points matching the magnetic measurement as presented in Figure 4.25. A good estimation of the velocity will indicate the right direction to follow, while a bad velocity estimation will drift inside the area.

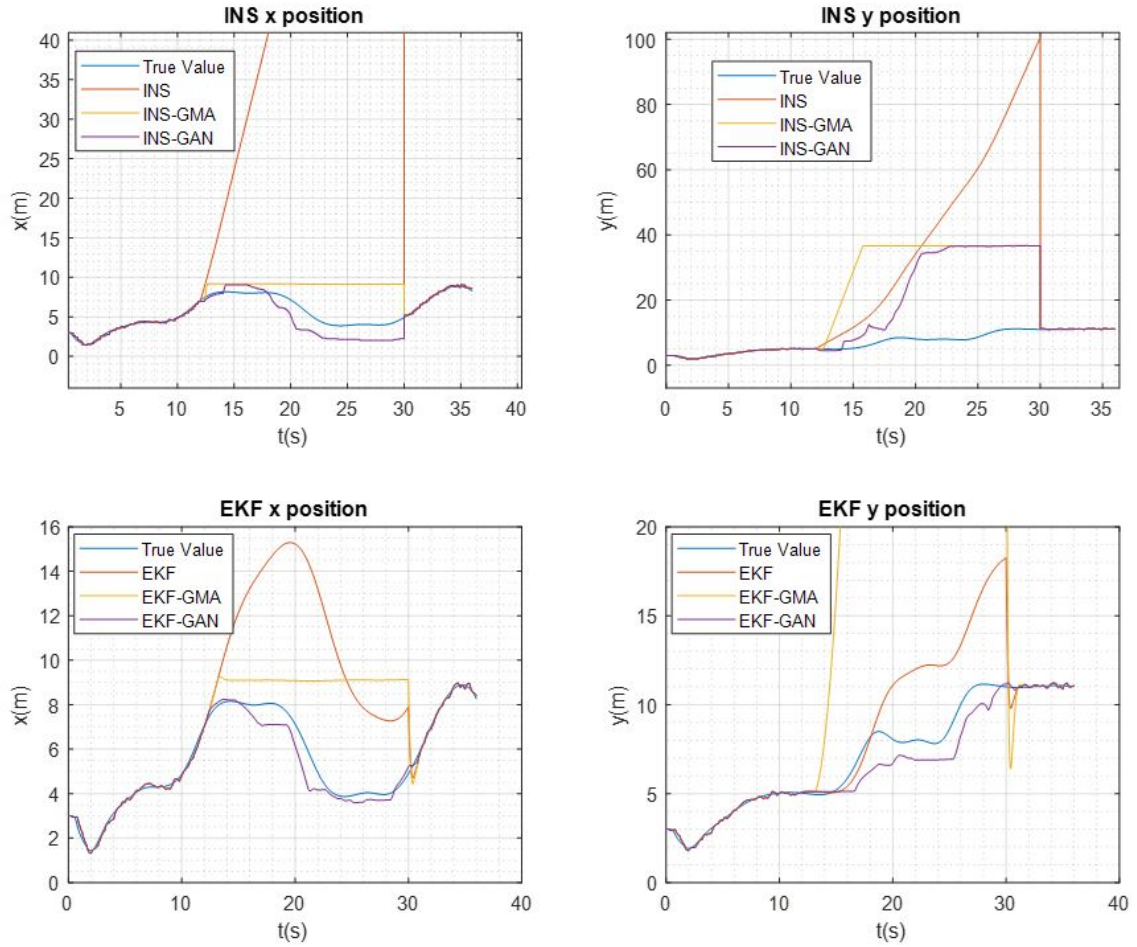


Figure 4.24 Trajectory S - INS and EKF estimation comparison

Additionally, by previously choosing a path to follow may help the algorithm to converge to the correct estimation if unique features of the field can be used. This refers to surface slopes, sources or concentrated points. It is completely different approaching the contour lines parallel than perpendicular, meaning that this characteristics may be considered before. Finally, over confidence in the Geomagnetic matching history may generate false clues when navigation around areas with no distinctive changes, and wrong maps may be completely useless for estimation, meaning that the quality and resolution of the map will define the accuracy of the estimations.



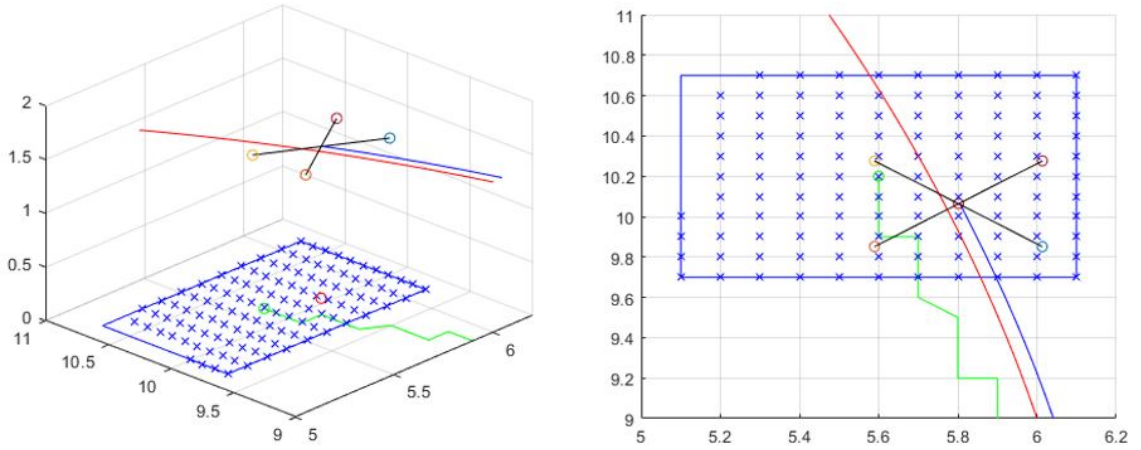


Figure 4.25 Flat Magnetic Area detected by the uncertainty area

#### 4.3.3.5. GAN with Velocity measurement and No GPS

An additional case is considered where velocity information is taken through sensors. In this specific case, the velocity information from GPS while the position estimation comes from the Geomagnetic estimator. As shown in Figures 4.27, 4.28 and 4.26, the position estimation improves when information of the velocity is available. As mentioned before, the velocity indicates the correct direction in the uncertainty area where the correct position is, specially when the NEDP algorithm falls in areas as shown in Figure 4.25 where all directions leads to positions with same magnetic value.

Last, by evaluating the position error, GPS based navigation still is the method with better accuracy, although the GAN algorithm supported by velocity has reduced error compared to the case where the velocity is estimated by the EKF. This can be observed in Table 4.2, where is noted that the position error is highly reduced. The information presented in this table refers to the evaluation of the root square of the square value of the position error for each case denoted. For the cases where only GPS position, and full GPS information drop occurs, still an interval of 12s to 30s is considered. At this last case, the only algorithm capable of keeping a close estimations of the real positions is the GAN proposed. At the same time, the INS algorithms shows its reduced performance in the estimations when no sources with reliable position information as GPS are available.

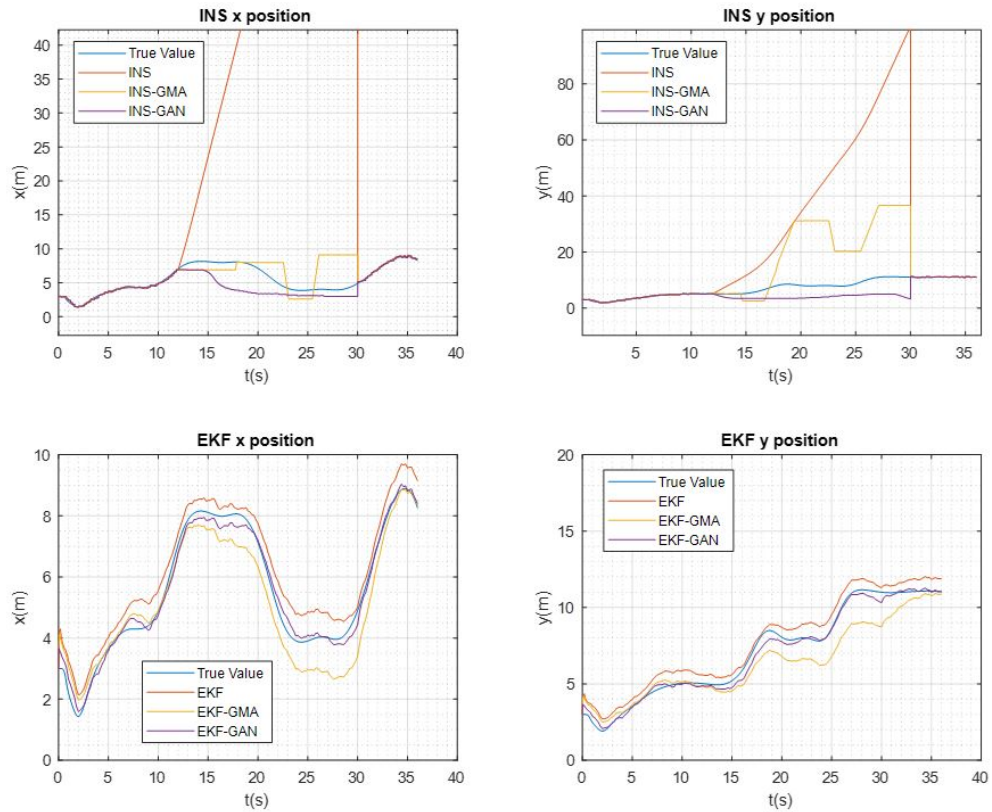


Figure 4.26 Trajectory S - INS and EKF Est. comparison with velocity measurement

Table 4.2

Error Metric Table of Estimator's performance

Position X (m)						
<b>GPS condition</b>	<b>INS</b>	<b>INSGMA</b>	<b>INSGNA</b>	<b>EKF</b>	<b>EKFGMA</b>	<b>EKFGAN</b>
<b>Pos</b>	N/A	N/A	N/A	0.09	0.141	0.090
<b>Pos+Vel</b>	N/A	N/A	N/A	0.09	0.01561	0.0172
<b>Vel (Pos. Drop)</b>	N/A	N/A	N/A	0.67	0.92	0.23
<b>Full GPS drop</b>	21.4	1.58	0.79	2.58	1.57	0.279
Position Y (m)						
<b>Pos</b>	N/A	N/A	N/A	0.0812	0.2356	0.1179
<b>Pos+Vel</b>	N/A	N/A	N/A	0.08	0.23	0.264
<b>Vel (Pos. Drop)</b>	N/A	N/A	N/A	0.60	0.61	0.1948
<b>Full GPS drop</b>	17.3	12.4	8.60	1.439	11.58	0.5452

To conclude, Geomagnetic Referencing models as Geomagnetic Matching and Contour approximations can be used to support GPS or replace it with higher reliability than INS during short periods of time. As presented along this Chapter 4, different combinations of this algorithms were performed with the objective of evaluate which combination is more robust specially at GPS denied intervals.

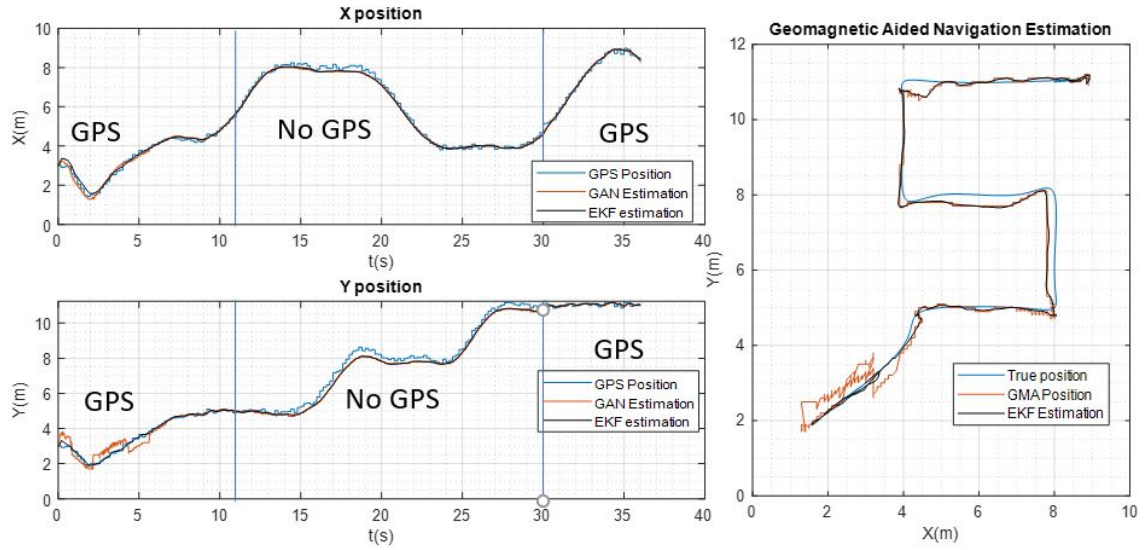


Figure 4.27 Trajectory S-GAN Est. with velocity measure/GPS drop at 12s-30s

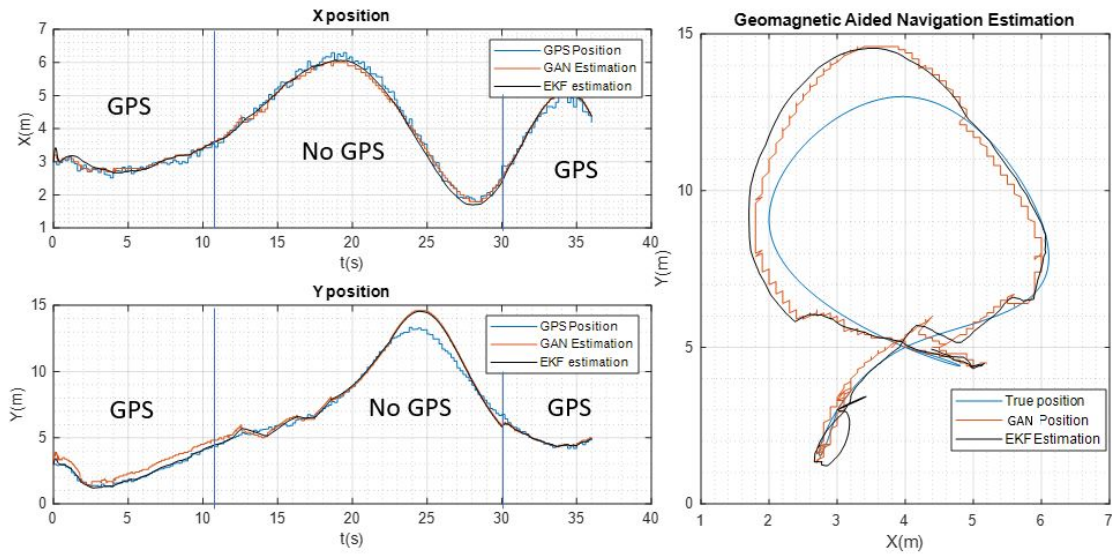
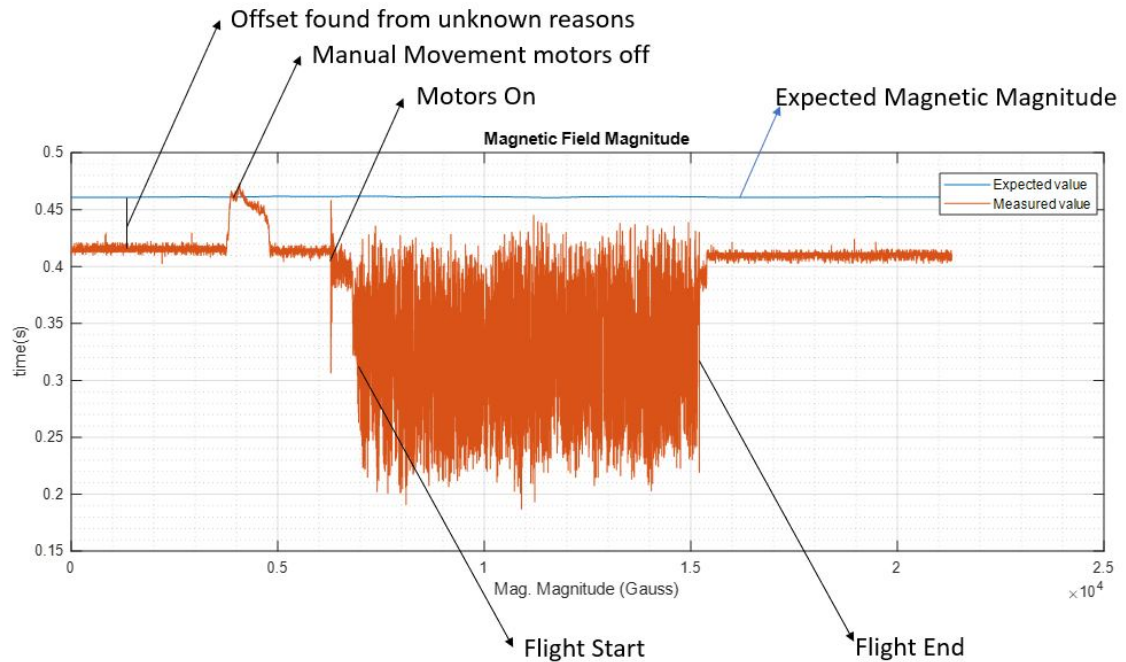


Figure 4.28 Trajectory O-GAN Est. with Velocity measure/GPS drop at 12s-30s

#### 4.4. Experimental Data Observations

At the post processing of the data gathered from different flights at the field, different conditions were found that severely affects the GAN algorithm. First and most important is the magnetic distortion to the field produced by the motors spinning. The motors are magnets with high amount of currents flowing through them generating magnetic fields that are still detected by the sensor, adding noise that affects the measurements.

The phenomenon the magnetic distortion can be observed in Figure 4.29 when the motors are turned on and the flight begins. The magnitude of the noise generated is huge compared to the expected value extracted from the map.



*Figure 4.29* Flight test Magnetic Data

Another observations is the initial offset compared to the expected value. This offset was found in several trials meaning that changes may exist due to Earth's rotation and translation cycles. Since the map was measured 5 months prior to any field testing, it is considered that there are possible variations of the field after a couple of months. It will be part of the continued investigation to observe the repeatability of the measurements and propose an alternative method to collect data for post processing as a ground vehicle with no disturbance sources capable of affecting the measurements.



## 5. Conclusions and Future Work

This research effort presents a Navigation algorithm using a Geomagnetic referenced architecture for local low altitude environments. The results presented in this documentation are supported by a user-friendly 3D simulation that explains the algorithms and identifies disturbances sources. This project establishes the basis for a Doctoral continued investigation work around the Geomagnetic Navigation planned at the Advanced Dynamics and Control Lab.

### 5.1. Development of Geomagnetic Maps

The construction of geomagnetic maps for navigations in local areas requires extensive effort and high-quality sensors to improve the position estimation of any Geomagnetic Aided Navigation method based on geomagnetic databases. A key factor to be considered is the model noise coming from the magnetic measurements. This means that maps will carry uncertainty when modeled, and this could represent increased error on implementations. Polynomial approximations of the field could be considered when sensors with low resolution and high noise are used for map characterization. Otherwise, an interpolated discrete reference should be considered. When considering scenarios with long distances, it is recommended to use the published databases depending on the mission; Geomagnetic anomaly data for low altitude flights and any available map at NOAA for high altitude maps as declination or magnetic strength maps.

### 5.2. Geomagnetic Aided Navigation

There exists a direct relation between a position in space and a geomagnetic contour that describes multiple points where the position in consideration is located. By implementing the GAN algorithm and testing each of the subsystems with the simulation environment proposed, multiple analytical outcomes were obtained. The Matching algorithm works as a correction method of the inertial navigation drift; hence, its information cannot estimate the position, although the magnetic history comparison provides it. Consequently, the existence of a position estimator based on sensors other than

IMU components is required. Here, this project proposes an initial approach based on the position estimation from the nearest contour point in the geomagnetic realm. Moreover, the importance of a reliable velocity estimation is noted because it can dictate the direction where the GAN algorithm can look inside the uncertainty area, specifically, when navigating in flat magnetic areas where no features can be detected. On the counterpart, with magnetic maps available and features detected, flight missions can be planned ahead to make use of these characteristics and improve the navigation. A proper analogy to this case is walking blinded thru a hallway blindfolded and using the sense of touch over a close wall to keep walking. The slopes of the magnetic field can be considered as the wall of the hallway. Last, if the algorithm is implemented along a controller, the tuning of the EKF estimation should be made along the tuning of the controller since the combination of this two tools defined how the vehicle moves in the environment.

### **5.3. Experimental Implementation**

Experimental implementations differ from simulation scenarios due to the nonlinear behaviors of the surroundings. This suggests that a simulation, although it can be close to reality, hardly will be exact. The main consideration for real implementation is noise, in measures, models, and possible disturbances from known sources. This can not be underestimated since most of the algorithms presented in this work are not deterministic but stochastic, implying changes of making a wrong estimation.

### **5.4. Simulation Environment**

Simulations are a powerful tool to understand behaviors and provide clues for the continued development of the algorithms. For this project, valuable information was obtained from the algorithms' visual representation rather than analysing numerical results. Even tho quantitative results were analyzed, qualitative evaluations were considered since GAN is proposed as alternative method understanding that GPS could be better, but not optimal or accessible for specific cases.

### 5.5. Future Work

To conclude this research, optional concepts are proposed to further review aiming for performance improvement of the algorithms proposed:

- Inclusion of velocity measurements from alternative sources as optical flow or ground speed estimation into the GAN algorithm to improve the position estimation by reducing or classifying importance sections in the uncertainty area
- Replace the NEDP estimation algorithm for robust stochastic methods as unscented kalman filters, or mass point techniques as particle filters
- Qualitative analysis of the influence of smaller sizes in the measurement history used in MAD algorithm computing.
- Trajectory planning methods based on geomagnetic features found in previously recorded maps
- Investigate optional approaches were the prior existence of a map is not required as SLAM algorithms, deep learning or artificial intelligence.

## REFERENCES

- Ardupilot. (2020). *Mission planner overview*. ArduPilot Dev Team. Retrieved from <https://ardupilot.org/planner/docs/mission-planner-overview.html>
- Balay, S. D. (2018). *Cryptochrome expression in the zebrafish retina: Potential implications for magnetoreception* (Ph.D. thesis). University of Alberta.
- Bevington, P. R., Robinson, D. K., Blair, J. M., Mallinckrodt, A. J., & McKay, S. (1993). Data reduction and error analysis for the physical sciences. *Computers in Physics*, 7(4), 415–416.
- Brindha, A., Balamurugan, S., & Venkatesh, P. (2011). Real time experiment to determine transfer function of quanser servo plant. In *2011 international conference on recent advancements in electrical, electronics and control engineering* (pp. 253–257).
- Britting, K. R. (1971). *Inertial navigation systems analysis*. Wiley-Interscience.
- Campbell, W. H. (2001). *Earth magnetism: a guided tour through magnetic fields*. Academic Press.
- Candy, J. V. (2016). *Bayesian signal processing: classical, modern, and particle filtering methods* (Vol. 54). John Wiley & Sons.
- Chang, L. (2017). Progress, Contribution and Challenges of Earth-Magnetism Navigation . *Automation, Control and Intelligent systems*, 5(1), 8-13.
- Courtillot, V. E., & Le Mouél, J.-L. (1976). Time variations of the earth's magnetic field with a period longer than two months. *Physics of the Earth and Planetary Interiors*, 12(2-3), 237–240.
- Cuenca Demidova, A. A., et al. (2016). *Diseño y construcción un cuadricóptero e implementación de un controlador de estabilidad para la aplicación de un algoritmo de vuelo autónomo* (B.S. thesis). Uniandes.
- Dai, Z., & Kang, C. (2014). Geomagnetic field aided inertial navigation using the sitan algorithm. In *The 2014 2nd international conference on systems and informatics (icsai 2014)* (pp. 79–83).
- Duan, X., Xiao, J., Qi, X., & Liu, Y. (2019). An ins/geomagnetic integrated navigation algorithm based on matching strategy and hierarchical filtering. *Electronics*, 8(4), 460.
- Ejaz, M., Iqbal, J., Ahsan, N., & Nawaz, A. (2009). Robust geomagnetic aided inertial navigation of underwater vehicles using the icp algorithm. In *2009 asia-pacific conference on computational intelligence and industrial applications (paciia)* (Vol. 1, pp. 257–262).

- Galarnyk, M. (2019, Nov). *68-95-99.7 rule for normal distribution*. Towards Data Science. Retrieved from <https://towardsdatascience.com/understanding-the-68-95-99-7-rule-for-a-normal-distribution-b7b7cbf760c2>
- Goldenber, F. (2006). Geomagnetic Navigation beyond the Magnetic Compass. *Position, Location, And navigation Symposium*, 684-694.
- Gordon, N., Ristic, B., & Arulampalam, S. (2004). Beyond the kalman filter: Particle filters for tracking applications. *Artech House, London*, 830(5), 1-4.
- High performance 6-axis mems motiontracking (Computer software manual No. ICM-20689). (2018, 3). (Rev. 2.2)
- Jing, X., Xiusheng, D., Xiaohui, Q., & Jianchen, W. (2018). Direction navigability analysis of geomagnetic field based on gabor filter. *Journal of Systems Engineering and Electronics*, 29(2), 378-385.
- Johnsen, S., Lohmann, K. J., & Warrant, E. J. (2020). Animal navigation: a noisy magnetic sense? *Journal of Experimental Biology*, 223(18).
- Kok, M., & Schön, T. B. (2016). Magnetometer calibration using inertial sensors. *IEEE Sensors Journal*, 16(14), 5679-5689.
- Lang, K. (2010). *The earth's double core*. Retrieved from [https://ase.tufts.edu/cosmos/print\\_images.asp?id=4](https://ase.tufts.edu/cosmos/print_images.asp?id=4)
- Lin, Y., Yan, L., & Tong, Q. (n.d.). Underwater geomagnetic navigation based on icp algorithm. In *2007 ieee international conference on robotics and biomimetics (robio)*.
- Liu, M., Wang, B., Deng, Z., & Fu, M. (2014). Improved iccp algorithm and its application in gravity matching aided inertial navigation system. In *Proceedings of the 33rd chinese control conference* (pp. 562-567).
- Liu, Y., Wu, M., Hu, X., & Xie, H. (2008). Geomagnetism aided inertial navigation system. In *2008 2nd international symposium on systems and control in aerospace and astronautics* (p. 1-5).
- Luo, S., Wang, Y., Liu, Y., & Hu, X. (2008). Research on geomagnetic-matching technology based on improved icp algorithm. In *2008 international conference on information and automation* (pp. 815-819).
- Luukkonen, T. (2011). Modelling and control of quadcopter. *Independent research project in applied mathematics, Espoo*, 22.
- Mian, A. A., & Daobo, W. (2008). Modeling and backstepping-based nonlinear control strategy for a 6 dof quadrotor helicopter. *Chinese Journal of Aeronautics*, 21(3), 261-268.

- Microstrain 3dm-gx4-45 datasheet (Computer software manual No. 4222037591). (2016).
- Mindling, G., & Bolton, R. (2008). *Usa air force tactical missiles*. Lulu. Retrieved from <https://books.google.com/books?id=P5WMDJ0HyP8C>
- Nelson, R. C., et al. (1998). *Flight stability and automatic control* (Vol. 2). WCB/McGraw Hill New York.
- Nygren, I. (2008). Robust and efficient terrain navigation of underwater vehicles. In *2008 IEEE/ION position, location and navigation symposium* (pp. 923–932).
- Oceanic, N., & Administration, A. (n.d.). *World magnetic model - maps of magnetic elements*. <https://www.ngdc.noaa.gov/geomag/WMM/image.shtml>.
- Rahok, S. A., Shikanai, Y., & Ozaki, K. (2011). Navigation using an environmental magnetic field for outdoor autonomous mobile robots. *Advanced Robotics*, 25(13-14), 1751–1771.
- Rivera, K. (2018). *Design and implementation of intelligent guidance algorithms for uav mission protection* (MSc. thesis). Embry-Riddle Aeronautical University.
- Sa, I., & Corke, P. (2011). Estimation and control for an open-source quadcopter. In *Proceedings of the australasian conference on robotics and automation 2011*.
- Stepanov, O., & Toropov, A. (2016). Nonlinear filtering for map-aided navigation part 2. trends in the algorithm development. *Gyroscopy and Navigation*, 7(1), 82–89.
- Storms, W. F. (2009). *Magnetic field aided indoor navigation* (MSc. thesis). Air Force Institute of Technology.
- Turan, B., & Kutay, A. T. (2016). Particle filter studies on terrain referenced navigation. In *2016 IEEE/ION position, location and navigation symposium (plans)* (pp. 949–954).
- Wei, L., Zhitian, W., Wu, M., & Hu, X. (2011). Geomagnetic matching technology based on iterative contour matching algorithm. In *Ieee 2011 10th international conference on electronic measurement & instruments* (Vol. 4, pp. 342–345).
- Woodman, O. J. (2007). *An introduction to inertial navigation* (Tech. Rep.). University of Cambridge, Computer Laboratory.
- Xiao, J., Duan, X., Qi, X., & Liu, Y. (2020). An improved iccp matching algorithm for use in an interference environment during geomagnetic navigation. *The Journal of Navigation*, 73(1), 56–74.
- Zhang, Y., Fan, Y., & Guo, Y. (2020). A geomagnetic positioning model based on naive bayes classifier. In *Proceedings of the 4th international conference on computer science and application engineering* (pp. 1–5).

- Zhang, Z. (1994). Iterative point matching for registration of free-form curves and surfaces. *International journal of computer vision*, 13(2), 119–152.
- Zhao, L., Gao, N., Huang, B., Wang, Q., & Zhou, J. (2014). A novel terrain-aided navigation algorithm combined with the tercom algorithm and particle filter. *IEEE Sensors Journal*, 15(2), 1124–1131.
- ZhongGuo, S., Jiuxiang, G., Jinsheng, Z., & Xiaoli, X. (2018). An improved method of geomagnetic aided inertial navigation algorithm with gyro and accelerometer error corrected online. In *Matec web of conferences* (Vol. 198, p. 02007).